AIMS Mathematics, 9(5): 12928–12963.
DOI: 10.3934/math.2024631
Received: 22 February 2024
Revised: 21 March 2024
Accepted: 26 March 2024
Published: 07 April 2024

https://www.aimspress.com/journal/Math

Research article

Configuration angle effect on the control process of an oscillatory rotor in 8-pole active magnetic bearings

Ali Kandil[1,2,*], Lei Hou[3], Mohamed Sharaf[4] and Ayman A. Arafa[1,5]

[1] Department of Applied and Computational Mathematics, Institute of Basic and Applied Sciences, Egypt-Japan University of Science and Technology (E-JUST), New Borg El-Arab City, 21934, Alexandria, Egypt
[2] Department of Physics and Engineering Mathematics, Faculty of Electronic Engineering, Menouf, 32952, Menoufia University, Egypt
[3] School of Astronautics, Harbin Institute of Technology, Harbin, 150001, China
[4] Industrial Engineering Department, College of Engineering, King Saud University, P.O. Box 800, Riyadh 11421, Saudi Arabia
[5] Department of Mathematics, Faculty of Science, Sohag University, 82524, Sohag, Egypt

* **Correspondence:** Email: ali.kandil@ejust.edu.eg, alikandil21@el-eng.menofia.edu.eg.

Abstract: In an active magnetic bearings (AMBs) model, every pair of opposite poles is aligned at an angle with the horizontal axis. In some configurations, there is a pair of poles which is in line with the horizontal axis. In other configurations, the same pair of poles might make a nonzero angle with the horizontal axis. This paper focused on the effect of changing such a configuration angle on the control process of an oscillatory rotor in an 8-pole active magnetic bearings model. Adopting the proportional-derivative (PD) control algorithm, the radial or Cartesian control techniques were applied. It was found that the rotor's oscillation amplitudes were not affected by the change in the configuration angle, even if its rotation speed and eccentricity were varied in the radial control scheme. However, the amplitudes were severely affected by the change in the configuration angle except at a specific angle in the Cartesian control scheme. The approximate modulating amplitudes and phases of the rotor's oscillations were extracted by the method of multiple-scales and a stability condition was tested based on the eigenvalues of the corresponding Jacobian matrix.

Keywords: configuration angle; 8-pole active magnetic bearings; rotor dynamics; quasiperiodic response; chaotic response; unbounded response

Mathematics Subject Classification: 34A34, 34C15, 34C23, 34C25, 34D20, 34E13, 37N15, 70B05, 70K05, 70K40, 70K42, 70K50

1. Introduction

Many academics from around the globe are interested in the dynamics of suspended rotors in an active magnetic bearings (AMBs) mechanism because of the rotors' ability to move without friction. Incorporating additional design parameters into the study to get closer to the real-world application makes rotor dynamics more difficult. Some examples of such design parameters are the rotor's weight, the number of stator poles, the control algorithm type, the presence of eddy currents, and so on. We should also enroll and discuss the configuration angle of the poles, another critical aspect. A steady-state solution to destabilize via saddle-node or Hopf bifurcation was studied by Ji and Hansen [1]. There were two stable solutions in the regime where several coexisting solutions were present. They looked at how the system's non-linear response was affected by imbalance eccentricity and the controller's proportional and derivative gains. Ji [2] examined the impact of delays on the system's non-linear dynamical behavior using a Jeffcott rotor that included an extra magnetic bearing located at the disc. To find out what a single Hopf bifurcation was, a center manifold was built. This study examined the relationship between the amplitude of the steady-state response and various parameters such as excitation amplitude, time delays, and control gains. Zhang and Zhan [3] employed the asymptotic perturbation approach to study chaotic dynamics and nonlinear oscillations in a rotor-AMBs system with 8-pole legs and time-varying stiffness. As a function of time, the AMB's stiffness was thought of as periodic. Amplitude oscillations with periods of 3, 4, 6, 7, and 8 were seen, along with quasiperiodic and chaotic motions.

Some papers dealt with approximating the AMBs model by using combinations of simple oscillator equations to ease the analysis. Li et al. [4] addressed the dynamical behavior of a parametrically stimulated Duffing-van der Pol oscillator under linear-plus-nonlinear state feedback control with a time delay. For the major parametric resonance situation, two slow-flow equations on the amplitude and phase of response were developed using the method of averaging in conjunction with truncation of Taylor expansions. Couzon and Der Hagopian [5] explored the active control of structures through AI capabilities, capitalizing on the great promise of merging neural networks with fuzzy logic. The study delved into the design, adjustment, and use of this sort of automatically adjustable nonlinear controller. In this case, a flexible rotor mounted on AMBs was controlled in its operational position by means of neuro-fuzzy control. Ji et al. [6] covered analysis methods, nonlinear vibrations caused by a rotor contacting auxiliary bearings, and other related topics in this literature review on nonlinear dynamics of magnetic bearing systems. Inoue and Sugawara [7,8] modeled the magnetic force by considering the electric current's second-order delay and the magnetic flux's first-order delay. They showed that the AMBs and PID (proportional-integral-derivative) control theory could enable a nonlinear analysis of a vertical rigid rotor. Eissa et al. [9] investigated a rotor-AMBs system with a stiffness that changed over time while being tuned and subjected to external excitations. In the studied resonance situation, Lyapunov's first approach was used to study the stability of the steady-state solution.

A connection between the Jeffcott rotor and AMBs model is analyzed in some research papers. Xu et al. [10] explored a Jeffcott rotor-AMBs model that incorporated time delays. The important findings were that the system's characteristic equation was singularity-satisfying, and the bifurcation between simple zero and zero-purely imaginary singularities was studied using center manifold

reduction and normal form. Li et al. [11] studied the non-linear behavior of a rotor under multi-parametric stimuli that was supported by AMBs. Two modes of a rotor-AMBs model were analyzed in response to the primary resonance case using the method of multiple scales. In AMBs with eight pole pairs, the nonlinear dynamics of the rotors suspended were studied by Yang et al. [12]. Three kinds of motions (in-unison modal, elliptic modal, and quasi-periodic) were discovered through research into the conservative free vibrations of general 2DOF nonlinear systems. A coaxial rotor system supported by two AMBs and in touch with two auxiliary bearings was the focus of the work done by Ebrahimi et al. [13], which aimed to forecast the nonlinear dynamic behavior of the system. They also included an examination of the contact forces felt by the auxiliary bearings and the inner shaft.

The stiffness types in AMBs model may create a problem in investigating the optimum conditions for the rotor's operations. Wu et al. [14] examined the complex nonlinear dynamics of rotor-AMBs with 16-pole legs and time-varying stiffness. A 2DOF nonlinear system that included the parametric excitation, quadratic and cubic nonlinearities was used to formulate the ensuing dimensionless equations of motion for the rotor-AMB system. Jha and Dasgupta [15] investigated the Sommerfeld effect, characterized by nonlinear jump phenomena of amplitude and rotor speed upon exceeding a critical nonlinear input around the critical speed, which was shown by eccentric shaft-disk systems with internal damping that were powered by an imperfect power source. Sun et al. [16] applied a cell mapping type method to analyze the nonlinear characteristics of an AMBs model. During the on-site commissioning experiment, this system was unstable under specific conditions and was stabilized after modifying the controller. Saeed and Kandil [17] presented a novel approach to controlling the rotor-AMBs model's lateral vibrations to enhance the system's vibrational behaviors. Thus, the rotor-AMB model was updated by incorporating the positive position feedback (PPF) controller and the standard proportional-derivative (PD) controller into the system under consideration. Hosseini and Yektanezhad [18] examined the primary resonance of a rotor that was both flexible and supported by AMBs. The gyroscopic effect was accounted for in the shaft model, but rotating inertia and shear deformation were ignored. This situation involved nonlinear boundary conditions and equations of motion.

Different types of controllers have been applied to suppress the vibrations of AMBs model. Kandil et al. [19] focused on a rotor-AMBs system with 16 poles for its oscillatory tendencies. Stabilizing the system's lateral oscillations, which were induced by the rotating disk eccentricity when the rotor's spinning speed was near to the system linear natural frequency, was achieved by using a regulated electromagnetic force generated by a typical proportional-derivative controller. Kandil [20] studied a constant-stiffness rotor-AMBs system with 16 poles. The imbalance between the rotor's horizontal and vertical displacements was demonstrated by deriving the equations of motion. Thus, the rotor could display a variety of whirls, including forward, backward, intermediate, or hybrid. Ma et al. [21] studied a nonlinear rotor-AMBs system with time-varying stiffness and 16-pole legs for its stability and Shilnikov-type multi-pulse jumping chaotic vibrations under mechanical-electric-electromagnetic excitations. The number and type of equilibrium points for the averaged equations were determined by applying certain coordinate transformations. To get around the standard PPF's two high peaks, Kandil and Hamed [22] introduced a tuned PPF controller that was combined with a PD controller to dampen vibrations in a system of rotor-AMBs with 16 poles and constant stiffness. Zhong et al. [23] proposed a unique rotor balancing method based on unsupervised deep learning. In the proposed network, additional convolution layers were used not only for the learning of the inverse mapping but also for identifying the unbalanced force without labeled data, in comparison to the supervised deep network. Kandil et al. [24] proposed a traditional nonlinear saturation controller (NSC) algorithm performance enhancement. With the use of a shaft encoder device, the NSC control unit could receive the rotor's measured speed, allowing for the implementation of a tuning mechanism that would result

in a tuned NSC. Saeed and Kandil [25] suggested comparing two distinct control schemes in a rotor-AMBs model. In the first approach, known as Cartesian control, the rotor's horizontal and vertical displacements determined the applied currents to the poles. Second, there was radial control, which involved regulating the currents that flowed based on the rotor's radial displacement.

Incorporating time-delay in the control process of AMBs model is very crucial to get near to the real-world application. Zhang and Xi [26] examined the vibration control of a rotor-AMBs system that incorporated a time delay. The results demonstrated that there was a periodic relationship between the time delay and the vibration amplitude as well as the stable zone. The nonlinear vibration of a rigid rotor hung by AMBs that was subjected to multiple excitations was suppressed by applying a time-delayed PD controller by Du et al. [27]. There were multi-solutions and jump phenomena, as shown by the results, but only under specific circumstances. Zhang et al. [28] investigated the effects of disturbance force, proportional gain, and differential gain on the soft-spring or hard-spring characteristics utilizing the multiple-scales method for an axial magnetic bearing-rotor system with a PD control. Yu et al. [29] established a mathematical model of the rotor of magnetic levitation turbomachinery, and an approach to PID control called a linear active disturbance rejection controller was introduced. This controller not only addressed previous common issues but also eliminated the need for the tedious parameter tuning that was used in the traditional nonlinear controller. Meher et al. [30] examined the steady-state and full transient characterization of the Sommerfeld effect in an unbalanced rotor-motor AMBs system considering the nonlinear bearing force. They obtained the precise voltage needed to pass through the resonance while the transient accelerated by the motor. Takam et al. [31] studied the dynamical behavior and static stability of AMBs constructed from n arbitrary pairs of electromagnetic coils. The obtained frequency response demonstrated that increasing the number n in the bearing and selecting a controller's proportional gain greater than a threshold value resulted in a decreased vibration amplitude.

According to Shilnikov-type multi-pulse chaotic dynamics, some researchers investigated the solutions nature in the AMBs model. Zhang et al. [32] focused on the time-varying stiffness in the 8-pole rotor-AMBs system, specifically on the Shilnikov-type multi-pulse chaotic dynamics. The numerical results revealed the presence of the characteristic Shilnikov-type multi-pulse chaotic motions in the studied model as well as a novel jumping phenomenon with time-varying stiffness. Li et al. [33] examined the bifurcations of multiple limit cycles in a rotor-AMBs model where the stiffness changed over time. It was discovered that the model, when subjected to various regulating conditions, exhibited limit cycles with time-varying stiffness at least 17, 19, 21, and 22 cycles. Zhang and Zu [34] studied both the steady and transient nonlinear dynamics of an 8-pole rotor-AMBs model with time-varying stiffness. They discovered solutions with 2, 3, 4, 5, 6, multi-, and quasiperiodic behaviors where it was possible to apply auto-controlling transient state chaos to both periodic and quasiperiodic motions in the steady-state behavior. Zhang et al. [35] focused on the rotor-AMBs model and how it displayed chaotic dynamics and global bifurcations. The given methods of selecting other adjacent spaces and applying the inner product further reduced the normal form to a simpler one. They showed that there were heteroclinic bifurcations and a Shilnikov-type single pulse homoclinic orbit. Zhang et al. [36] studied the chaotic dynamics of a rotor-AMBs model with time-varying stiffness and 16-pole legs using the asymptotic perturbation method. The frequency response study revealed that the studied model exhibited both hardening-type and softening-type nonlinearities.

Some recent papers discussed including deep learning in controlling the AMBs model. Yang et al. [37] proposed the deep reinforcement learning based model calibration frame (DRLMC) as a model calibration method. They initiated the dynamic life cycle modeling of a magnetic bearing with damage degradation where a Markov decision process (MDP) was then used to model the calibration process,

and the degradation parameters were inferred via reinforcement learning (RL). Xu et al. [38] presented a universal dynamic model and solution scheme to use both static and dynamic eccentricities in a single, succinct air-gap length model to obtain the magnetic pull force and the analytical and numerical computation approaches in an electrical rotor model. Wei et al. [39] proposed a method for modeling the rotor dynamics based on the rotor's structural properties to address the problem of the magnetic levitation turbo rotor system's modal self-excited oscillation. The results of the experiments confirmed the accuracy and effectiveness of the proposed system. Saket and Keogh [40] described the novel contact control method in AMBs system based on measuring the strain in the stator that resulted from the contact between the rotor and the touchdown bearings. With the help of the measured data, they could determine the phase shifts and frequency dependent magnetic bearing control forces that allowed the rotor to recover from contact. Liu et al. [41] investigated the clearance compatibility of gas bearings and active magnetic bearings to develop a hybrid bearing design that combined the best of both functions of gas and magnetic bearings. Wei et al. [42] dealt with the control of stability of shock-excited disturbance in high-speed magnetic levitation turbomolecular pumps to reduce the impact of external low-frequency disturbing force on a magnetic levitation turbomolecular pump. Jiang et al. [43] designed a carbon dioxide heat pump system with a centrifugal compressor where a synchronous motor with a high-speed permanent magnet drove the compressor directly. The motor was equipped with active magnetic bearings and two-stage impellers on either side. Han et al. [44] obtained an effective solution for vibration control of the AMB-flexible support structure by modifying the structure according to the method proposed, where this modification reduced base vibration under the excitation of rotor rotation frequency.

An 8-pole AMBs model with an oscillating rotor was introduced in this research along with a study on how the configuration angle affected the control process. The popular PD control algorithm-based radial and Cartesian control schemes were chosen. We have shown that the rotor's oscillation amplitudes were not affected by the change in the configuration angle, even if its rotation speed and eccentricity were varied in the radial control scheme. Furthermore, the amplitudes were severely affected by the change in the configuration angle except at a specific angle in the Cartesian control scheme. The rotor's oscillations were governed by a system of two ordinary differential equations that are nonlinear. A stability test was constructed by checking the associated Jacobian matrix's eigenvalues, and the approximate modulating amplitudes and phases of the rotor's oscillations were retrieved using the multiple-scales approach. The current study provides a broader view of the authors' investigation by including various numerical and analytical responses.

2. Modelling the motion of an 8-pole rotor-AMBs model

The vertically supported 8-pole rotor-AMBs model is shown in Figure 1. The motion equations of the rotor are written as [45]:

$$M\ddot{x} + \delta\dot{x} - R_x = ME\Omega^2 \cos(\Omega t), \tag{1}$$

$$M\ddot{y} + \delta\dot{y} - R_y = ME\Omega^2 \sin(\Omega t), \tag{2}$$

where x and y are the horizontal and vertical displacements of the rotor, respectively, the dot refers to differentiation with respect to time t, and R_x and R_y represent the nonlinear magnetic restoring resultant forces in the x and y directions, respectively. Additionally, the symbols M, E, and Ω are the mass, eccentricity, and rotating speed of the rotor, respectively, while δ is the presumed viscous damping factor. Due to the mechanical design, the angle between the central axes of any two consecutive

poles is $\alpha = \pi/4$.

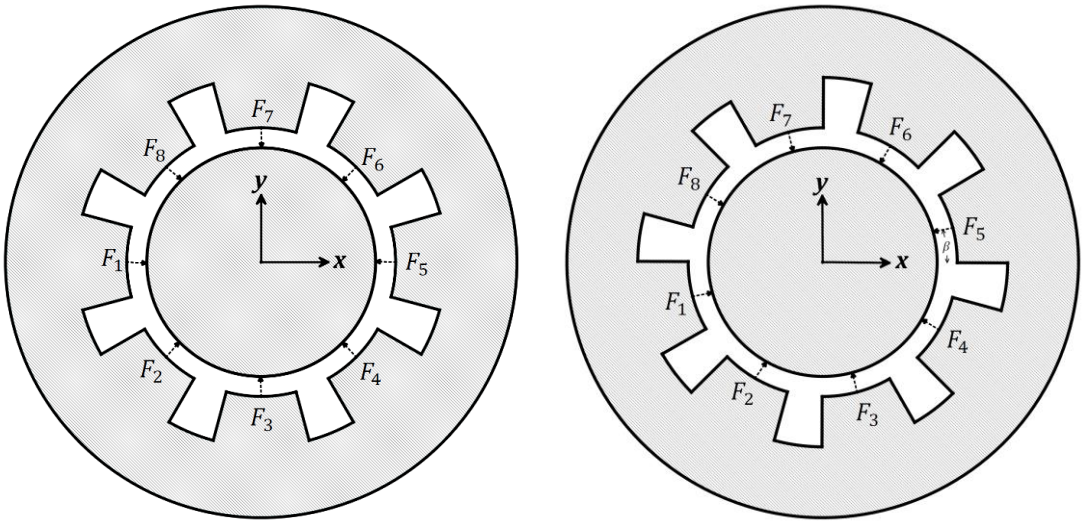

Figure 1. Vertically supported 8-pole rotor-AMBs model: (a) initial configuration at $\beta = 0°$; (b) another configuration at $\beta > 0°$.

As shown in Figure 1(a), the poles are arranged in an initial configuration at $\beta = 0°$, i.e., the central axes of the first and fifth poles are horizontal. In addition, Figure 1(b) shows another configuration at $\beta > 0°$, or in other words, the central axes of the first and fifth poles are inclined with the horizontal axis by an angle β. Moreover, every pole (electromagnet) of the eight poles can induce an electromagnetic force F_n $(n = 1, 2, \cdots, 8)$ according to the relation:

$$F_n = K\left(\frac{I_0 - I_n}{C_0 - C_n}\right)^2, \tag{3}$$

where K is a constant value related to the design parameters of each pole's coil, I_0 is the preliminary current for an initial suspension, I_n is the control current which is adjusted through a feedback control, and C_0 and C_n are the static and dynamic gaps, respectively, between the rotor and every pole. The dynamic gap C_n can be defined as

$$C_n = x\cos\big((n-1)\alpha + \beta\big) + y\sin\big((n-1)\alpha + \beta\big), \tag{4}$$

where α is the angle between any two poles and β is the configuration angle. The nonlinear magnetic restoring resultant forces R_x and R_y can be computed as

$$R_x = \sum_{j=1}^{8} F_j \cos\big((j-1)\alpha + \beta\big), \tag{5}$$

$$R_y = \sum_{j=1}^{8} F_j \sin\big((j-1)\alpha + \beta\big). \tag{6}$$

The control current I_n is generated depending on the most suitable way to control such a model that is the proportional-derivative (PD) controller. Hence, we are introducing two different strategies, the radial PD control method and the Cartesian PD control method, and will explore whether there is a relation between the applied control strategy and the configuration angle β.

2.1. The relation between the radial PD control technique and the configuration angle β

The proportional-derivative (PD) controller is one of the most robust controllers in AMBs models as was stated in [1–3,6,9,14]. It can be enrolled into the model's equations of motion by being analytically differentiated and approximated in an easy manner. In addition, it can give acceptable levels of vibration suppression via adjusting its simple gains. In this paper, our focus is not on the application of PD on AMBs because it was used before. Our focus is on exploring the effect of changing the configuration angle on the PD control process of AMBs. The radial PD control method adjusts the control current I_n in order to be a function of the rotor's dynamic gap C_n and its derivative $\dot{C}_n$ as follows

$$I_n = g_1 C_n + g_2 \dot{C}_n, \tag{7}$$

where g_1 and g_2 denote the proportional and derivative gains, respectively. Substituting Eqs (4) and (7) into Eq (3) gives us the approximated forms of Eqs (5) and (6) up to the third-order expansions. Afterward, inserting the resulting R_x and R_y into Eqs (1) and (2) yields

$$\ddot{x} + \zeta_r \dot{x} + \omega_r^2 x + \varrho_1(x^3 + xy^2) + \varrho_2(\dot{x}y^2 + 2xy\dot{y} + 3x^2\dot{x}) + \varrho_3(x\dot{y}^2 + 2\dot{x}y\dot{y} + 3x\dot{x}^2) = e\Omega^2 \cos(\Omega t), \tag{8}$$

$$\ddot{y} + \zeta_r \dot{y} + \omega_r^2 y + \varrho_1(y^3 + x^2y) + \varrho_2(x^2\dot{y} + 2x\dot{x}y + 3y^2\dot{y}) + \varrho_3(\dot{x}^2y + 2x\dot{x}\dot{y} + 3y\dot{y}^2) = e\Omega^2 \sin(\Omega t), \tag{9}$$

where the parameters e, ζ_r, ω_r^2, ϱ_1, ϱ_2, and ϱ_3 are given in Appendix A. The detailed derivation of Eqs (8) and (9) is given in Appendix C. To get an approximate solution of the nonlinear DEs Eqs (8) and (9), the multiple-scales procedure [46] has been utilized. The dimensionless horizontal and vertical rotor's oscillations $x(t)$ and $y(t)$ can be expressed as

$$x(t;\varepsilon) = x_0(T_0, T_1) + \varepsilon x_1(T_0, T_1) + O(\varepsilon^2), \tag{10}$$

$$y(t;\varepsilon) = y_0(T_0, T_1) + \varepsilon y_1(T_0, T_1) + O(\varepsilon^2), \tag{11}$$

where T_0 and T_1 are two different time scales and ε is a perturbation parameter. The adopted real-time ordinary-derivative is converted to multiple-times partial-derivatives to be

$$\frac{d^j}{dt^j} = \left(\sum_{i=0}^{\infty} \varepsilon^i D_i\right)^j, \tag{12}$$

where we need in this work the second derivative as the highest one, so $j = 1, 2$, and also the adopted partial derivatives are $D_0 = \partial/\partial T_0$ and $D_1 = \partial/\partial T_1$, so $i = 1, 2$. A suitable scaling with ε is imposed on specific parameters of Eqs (8) and (9) such that

$$\zeta_r = \varepsilon\tilde{\zeta}_r,\ \varrho_1 = \varepsilon\tilde{\varrho}_1,\ \varrho_2 = \varepsilon\tilde{\varrho}_2,\ \varrho_3 = \varepsilon\tilde{\varrho}_3,\ e = \varepsilon\tilde{e}. \tag{13}$$

Substituting Eqs (10)–(13) into Eqs (8) and (9) and following the procedure of multiple scales can lead us to the following autonomous system governing the rotor's motion amplitudes (a_x and a_y) and phases (ψ_x and ψ_y):

$$\dot{a}_x = -\left(\frac{\zeta_r}{2}\right) a_x - \left(\frac{\varrho_1 + \varrho_3\omega_r^2}{8\omega_r}\right) a_x a_y^2 \sin(2\psi_{xy}) - \left(\frac{\varrho_2}{8}\right) a_x a_y^2 \cos(2\psi_{xy}) - \left(\frac{3\varrho_2}{8}\right) a_x^3 - \left(\frac{\varrho_2}{4}\right) a_x a_y^2 + \left(\frac{e\Omega^2}{2\omega_r}\right) \sin\psi_x, \tag{14}$$

$$\dot{\psi}_x = \Omega - \omega_r - \left(\frac{\varrho_1+\varrho_3\omega_r^2}{8\omega_r}\right)a_y^2\cos(2\psi_{xy}) + \left(\frac{\varrho_2}{8}\right)a_y^2\sin(2\psi_{xy}) - \left(\frac{3\varrho_1+3\varrho_3\omega_r^2}{8\omega_r}\right)a_x^2 - \left(\frac{\varrho_1+\varrho_3\omega_r^2}{4\omega_r}\right)a_y^2 + \left(\frac{e\Omega^2}{2\omega_r}\right)\frac{\cos\psi_x}{a_x}, \tag{15}$$

$$\dot{a}_y = -\left(\frac{\zeta_r}{2}\right)a_y + \left(\frac{\varrho_1+\varrho_3\omega_r^2}{8\omega_r}\right)a_x^2a_y\sin(2\psi_{xy}) - \left(\frac{\varrho_2}{8}\right)a_x^2a_y\cos(2\psi_{xy}) - \left(\frac{3\varrho_2}{8}\right)a_y^3 - \left(\frac{\varrho_2}{4}\right)a_x^2a_y - \left(\frac{e\Omega^2}{2\omega_r}\right)\cos\psi_y, \tag{16}$$

$$\dot{\psi}_y = \Omega - \omega_r - \left(\frac{\varrho_1-\varrho_3\omega_r^2}{8\omega_r}\right)a_x^2\cos(2\psi_{xy}) - \left(\frac{\varrho_2}{8}\right)a_x^2\sin(2\psi_{xy}) - \left(\frac{3\varrho_1+\varrho_3\omega_r^2}{8\omega_r}\right)a_y^2 - \left(\frac{\varrho_1+\varrho_3\omega_r^2}{4\omega_r}\right)a_x^2 + \left(\frac{e\Omega^2}{2\omega_r}\right)\frac{\sin\psi_y}{a_y}, \tag{17}$$

where $\psi_{xy} = \psi_x - \psi_y$. The fixed points of Eqs (14)–(17) can be found by assuming that $\dot{a}_x = \dot{a}_y = \dot{\psi}_x = \dot{\psi}_y = 0$. Hence, the resulting system of nonlinear equations is solved numerically to find the set of fixed points $\{a_{xs},\ a_{ys},\ \psi_{xs},\ \psi_{ys}\}$. This set of fixed points is tested for stability by proposing the following:

$$a_x = a_{xs} + \Delta a_x, \tag{18}$$

$$\psi_x = \psi_{xs} + \Delta\psi_x, \tag{19}$$

$$a_y = a_{ys} + \Delta a_y, \tag{20}$$

$$\psi_y = \psi_{ys} + \Delta\psi_y, \tag{21}$$

where the set $\{\Delta a_x,\ \Delta a_y,\ \Delta\psi_x,\ \Delta\psi_y\}$ are small changes added to the set $\{a_{xs},\ a_{ys},\ \psi_{xs},\ \psi_{ys}\}$. Inserting Eqs (18)–(21) into Eqs (14)–(17) and keeping only the linear terms in the expansions of the set $\{\Delta a_x,\ \Delta a_y,\ \Delta\psi_x,\ \Delta\psi_y\}$, we get

$$\left[\Delta\dot{a}_x \quad \Delta\dot{\psi}_x \quad \Delta\dot{a}_y \quad \Delta\dot{\psi}_y\right]^T = \boldsymbol{J}[\Delta a_x \quad \Delta\psi_x \quad \Delta a_y \quad \Delta\psi_y]^T, \tag{22}$$

where $\boldsymbol{J}$ is the Jacobian matrix, and Appendix B contains its entries. Asymptotically stable fixed points are those that have all their real parts in the Jacobian eigenvalues being negative. They are considered unstable otherwise.

2.2. The relation between the Cartesian PD control and the configuration angle β

Herein, the control current I_n is to be adjusted as

$$I_1 = I_8 = -I_4 = -I_5 = g_1x + g_2\dot{x}, \tag{23}$$

$$I_2 = I_3 = -I_6 = -I_7 = g_1y + g_2\dot{y}. \tag{24}$$

Substituting Eqs (23) and (24) into Eq (3), then inserting the third-order expansions of Eqs (5) and (6) into Eqs (1) and (2) lead to the following dimensionless system of DEs according to the same normalization process done in subsection 2.1.

$$\ddot{x} + \zeta_c\dot{x} + \omega_c^2x + \eta_1x^3 + \eta_2xy^2 + \eta_3x^2\dot{x} + \eta_4\dot{x}y^2 + \eta_5x\dot{x}^2 + \eta_6x\dot{y}^2 + \eta_7xy\dot{y} + \eta_8\dot{y}$$
$$+\eta_9y + \eta_{10}x^2y + \eta_{11}y^3 + \eta_{12}x^2\dot{y} + \eta_{13}y^2\dot{y} + \eta_{14}\dot{x}^2y - \eta_{14}y\dot{y}^2$$

$$+\eta_{15}x\dot{x}y = e\Omega^2\cos(\Omega t), \tag{25}$$

$$\ddot{x} + \zeta_c\dot{x} + \omega_c^2 x + \eta_1 x^3 + \eta_2 xy^2 + \eta_3 x^2\dot{x} + \eta_4\dot{x}y^2 + \eta_5 x\dot{x}^2 + \eta_6 x\dot{y}^2 + \eta_7 xy\dot{y} + \eta_8\dot{y}$$
$$+\eta_9 y + \eta_{10}x^2 y + \eta_{11}y^3 + \eta_{12}x^2\dot{y} + \eta_{13}y^2\dot{y} + \eta_{14}\dot{x}^2 y - \eta_{14}y\dot{y}^2$$
$$+\eta_{15}x\dot{x}y = e\Omega^2\cos(\Omega t), \tag{26}$$

where the parameters ζ_c, ω_c^2, and η_1,…, η_{15} depend directly on the configuration angle β and are given in Appendix A. Using the multiple-scales approach [46], an approximate solution of the nonlinear DEs Eqs (25) and (26) has been obtained. The rotor's modulated amplitudes (a_x and a_y) and phases (ψ_x and ψ_y) are governed by the given autonomous system:

$$\begin{aligned}\dot{a}_x = &-\left(\frac{\zeta_c}{2}\right)a_x - \left(\frac{\eta_2 - \eta_6\omega_c^2}{8\omega_c}\right)a_x a_y^2\sin(2\psi_{xy}) - \left(\frac{\eta_{10} + 3\eta_{14}\omega_c^2}{8\omega_c}\right)a_x^2 a_y\sin\psi_{xy}\\ &- \left(\frac{3\eta_{11} - \eta_{14}\omega_c^2}{8\omega_c}\right)a_y^3\sin\psi_{xy} - \left(\frac{\eta_9}{2\omega_c}\right)a_y\sin\psi_{xy}\\ &+ \left(\frac{\eta_4 - \eta_7}{8}\right)a_x a_y^2\cos(2\psi_{xy}) - \left(\frac{\eta_{12} + \eta_{15}}{8}\right)a_x^2 a_y\cos\psi_{xy}\\ &- \left(\frac{\eta_{13}}{8}\right)a_y^3\cos\psi_{xy} - \left(\frac{\eta_8}{2}\right)a_y\cos\psi_{xy} - \left(\frac{\eta_3}{8}\right)a_x^3 - \left(\frac{\eta_4}{4}\right)a_x a_y^2\\ &+ \left(\frac{e\Omega^2}{2\omega_c}\right)\sin\psi_x,\end{aligned} \tag{27}$$

$$\begin{aligned}\dot{\psi}_x = \Omega - \omega_c &- \left(\frac{\eta_2 - \eta_6\omega_c^2}{8\omega_c}\right)a_y^2\cos(2\psi_{xy}) - \left(\frac{3\eta_{10} + \eta_{14}\omega_c^2}{8\omega_c}\right)a_x a_y\cos\psi_{xy}\\ &- \left(\frac{3\eta_{11} - \eta_{14}\omega_c^2}{8\omega_c}\right)\frac{a_y^3\cos\psi_{xy}}{a_x} - \left(\frac{\eta_9}{2\omega_c}\right)\frac{a_y\cos\psi_{xy}}{a_x}\\ &- \left(\frac{\eta_4 - \eta_7}{8}\right)a_y^2\sin(2\psi_{xy}) - \left(\frac{3\eta_{12} + \eta_{15}}{8}\right)a_x a_y\sin\psi_{xy} + \left(\frac{\eta_{13}}{8}\right)\frac{a_y^3\sin\psi_{xy}}{a_x}\\ &+ \left(\frac{\eta_8}{2}\right)\frac{a_y\sin\psi_{xy}}{a_x} - \left(\frac{3\eta_1 + \eta_5\omega_c^2}{8\omega_c}\right)a_x^2 - \left(\frac{\eta_2 + \eta_6\omega_c^2}{4\omega_c}\right)a_y^2 + \left(\frac{e\Omega^2}{2\omega_c}\right)\frac{\cos\psi_x}{a_x},\end{aligned} \tag{28}$$

$$\begin{aligned}\dot{a}_y = &-\left(\frac{\zeta_c}{2}\right)a_y + \left(\frac{\eta_2 - \eta_6\omega_c^2}{8\omega_c}\right)a_x^2 a_y\sin(2\psi_{xy}) - \left(\frac{\eta_{10} + 3\eta_{14}\omega_c^2}{8\omega_c}\right)a_x a_y^2\sin\psi_{xy}\\ &- \left(\frac{3\eta_{11} - \eta_{14}\omega_c^2}{8\omega_c}\right)a_x^3\sin\psi_{xy} - \left(\frac{\eta_9}{2\omega_c}\right)a_x\sin\psi_{xy}\\ &+ \left(\frac{\eta_4 - \eta_7}{8}\right)a_x^2 a_y\cos(2\psi_{xy}) + \left(\frac{\eta_{12} + \eta_{15}}{8}\right)a_x a_y^2\cos\psi_{xy}\\ &+ \left(\frac{\eta_{13}}{8}\right)a_x^3\cos\psi_{xy} + \left(\frac{\eta_8}{2}\right)a_x\cos\psi_{xy} - \left(\frac{\eta_3}{8}\right)a_y^3 - \left(\frac{\eta_4}{4}\right)a_x^2 a_y\\ &- \left(\frac{e\Omega^2}{2\omega_c}\right)\cos\psi_y,\end{aligned} \tag{29}$$

$$\begin{aligned}\dot{\psi}_y = \Omega - \omega_c - \left(\frac{\eta_2 - \eta_6\omega_c^2}{8\omega_c}\right)a_x^2\cos(2\psi_{xy}) + \left(\frac{3\eta_{10} + \eta_{14}\omega_c^2}{8\omega_c}\right)a_x a_y\cos\psi_{xy} \\ + \left(\frac{3\eta_{11} - \eta_{14}\omega_c^2}{8\omega_c}\right)\frac{a_x^3\cos\psi_{xy}}{a_y} + \left(\frac{\eta_9}{2\omega_c}\right)\frac{a_x\cos\psi_{xy}}{a_y} \\ + \left(\frac{\eta_4 - \eta_7}{8}\right)a_x^2\sin(2\psi_{xy}) + \left(\frac{3\eta_{12} - \eta_{15}}{8}\right)a_x a_y\sin\psi_{xy} + \left(\frac{\eta_{13}}{8}\right)\frac{a_x^3\sin\psi_{xy}}{a_y} \\ + \left(\frac{\eta_8}{2}\right)\frac{a_x\sin\psi_{xy}}{a_y} - \left(\frac{3\eta_1 + \eta_5\omega_c^2}{8\omega_c}\right)a_y^2 - \left(\frac{\eta_2 + \eta_6\omega_c^2}{4\omega_c}\right)a_x^2 + \left(\frac{e\Omega^2}{2\omega_c}\right)\frac{\sin\psi_y}{a_y}.\end{aligned} \tag{30}$$

The fixed points of Eqs (27)–(30) are computed by letting $\dot{a}_x = \dot{a}_y = \dot{\psi}_x = \dot{\psi}_y = 0$, then the resulting system of nonlinear equations is solved numerically to find the set of fixed points $\{a_{xs},\ a_{ys},\ \psi_{xs},\ \psi_{ys}\}$. The stability of the gained fixed points can be tested by substituting Eqs (18)–(21) into Eqs (27)–(30), then following the same stability analysis done in subsection 2.1 to derive an equation in the following form:

$$\left[\Delta\dot{a}_x \quad \Delta\dot{\psi}_x \quad \Delta\dot{a}_y \quad \Delta\dot{\psi}_y\right]^T = \boldsymbol{L}[\Delta a_x \quad \Delta\psi_x \quad \Delta a_y \quad \Delta\psi_y]^T, \tag{31}$$

where the entries of the newly deduced Jacobian matrix $\boldsymbol{L}$ are given in Appendix B.

3. Analytical results and discussion

The figures indicating the effect of the configuration angle β and different parameters of the studied model for either control scheme are included in this section. Furthermore, there are adopted values for some other parameters such as: $p = 1.22,\ d = 0.005,\ \delta_1 = 0.001$, and $e = 0.01$, unless otherwise mentioned. The curves that are plotted in solid form denote stable paths of equilibrium amplitudes, while the dashed curves refer to unstable paths of equilibrium amplitudes based upon the stability criteria discussed in Eqs (22) and (31).

3.1. Results on the relation between the configuration angle β and the radial control scheme

Herein, we are going to plot the figures depending on the analysis done in Section 2.1. In Eqs (8) and (9), there are nonlinear coefficients $\varrho_1,\ \varrho_2$, and ϱ_3 that are given in Appendix A as functions of the parameters $p,\ d$, and β. These nonlinear coefficients are plotted as functions of the configuration angle β (in a range from $0°$ to $45°$) keeping p and d fixed at specific values. This is to investigate the dependence of such coefficients on the angle β as shown in Figure 2. The nonlinear coefficients $\varrho_1,\ \varrho_2$, and ϱ_3 are not affected by the change in the angle β in the radial control method. They change only if the parameters p and d are varied. This can be explained as the sinusoidal functions of β, defined in the equations of $\varrho_1,\ \varrho_2$, and ϱ_3, cancel each other as if they do not exist.

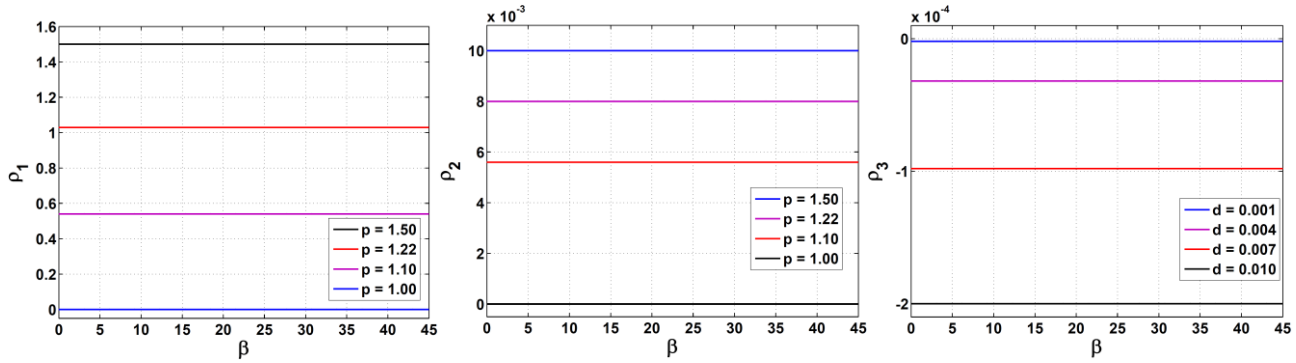

(a) (b) (c)

Figure 2. The relations between ϱ_1, ϱ_2, ϱ_3 vs. the configuration angle β: (a) ϱ_1 vs. β at $d = 0.005$ and different p, (b) ϱ_2 vs. β at $d = 0.005$ and different p, (c) ϱ_3 vs. β at $p = 1.22$ and different d.

As can be seen from Eqs (9) and (10), the displacements $x(t)$ and $y(t)$ are governed by symmetrical differential equations in the parameters' values. The only difference is that they are excited by $\cos(\Omega t)$ and $\sin(\Omega t)$, respectively, where this will affect the solutions' phases only without affecting the solutions' amplitudes. Moreover, computing the amplitudes a_x and a_y in Eqs (14)–(17) gives us identical values for both amplitudes. Hence, we have merged the two identical amplitude plots into one figure as will be shown. For different values of the angle β (0°, 10°, 22.5°, 30°, and 45°), the rotor's equilibrium amplitudes a_x and a_y of Eqs (14)–(17) have been plotted in response to the change of the rotor's rotation speed Ω and its eccentricity e as shown in Figure 3. It is also assured, as in Figure 2, that the amplitudes a_x and a_y are not affected by the change in the angle β. On the other hand, raising the rotor's eccentricity e can enhance the nonlinear behavior denoted by the curve's bending to the right due to the hardening behavior of the electromagnetic restoring forces.

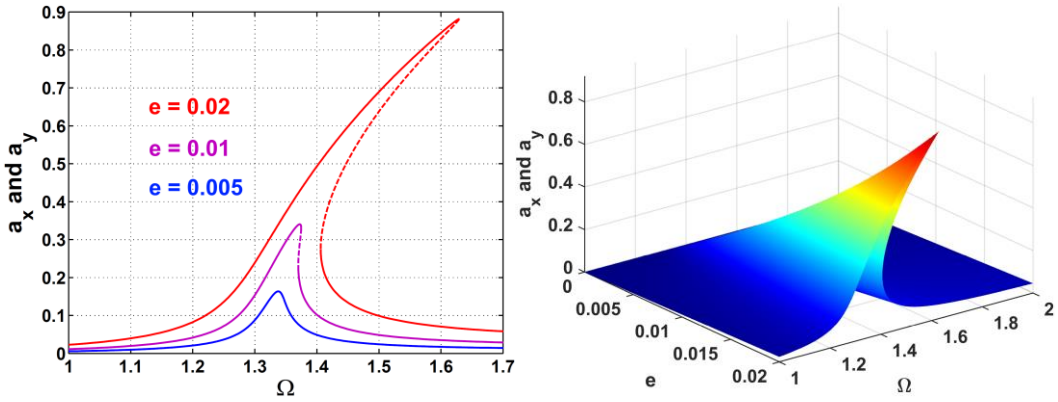

(a) (b)

Figure 3. The rotor's amplitudes a_x and a_y vs. its rotation speed Ω at different values of its eccentricity e: (a) a_x and a_y vs. Ω, (b) 3D surface of a_x and a_y vs. Ω and e.

In addition, the relations of the rotor's equilibrium amplitudes a_x and a_y versus its eccentricity e at different values of its rotation speed Ω and different configuration angles β are shown in Figure 4.

The crucial role of Ω is when it increases, the response curve begins to have unstable branches as shown in the figure. Each unstable branch is confined between two saddle-node bifurcation points that switch the stability condition of the curve. It seems that the unstable branch is enlarged in proportion to increasing the rotation speed Ω, where a possibility of an amplitude jump can happen between two stable branches.

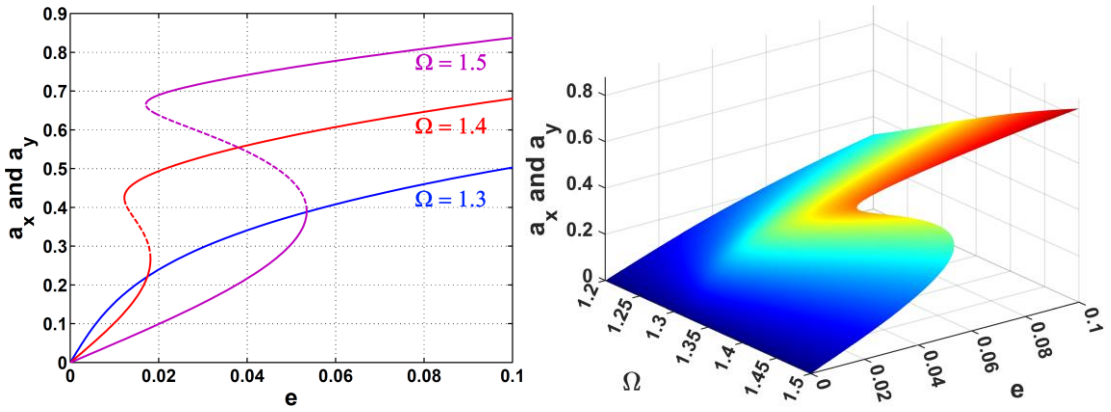

Figure 4. The rotor's amplitudes a_x and a_y vs. its eccentricity e at different values of its rotation speed Ω: (a) a_x and a_y vs. e, (b) 3D surface of a_x and a_y vs. e and Ω.

The effect of varying the position-gain p on the rotor's equilibrium amplitudes in response to its rotation speed Ω is depicted in Figure 5. As can be seen, the amplitudes get larger in the case of raising the position-gain p along with the rotation speed Ω. This gives us a clue about higher oscillation amplitudes to make the rotor impact with the pole legs. The unstable branches at lower values of p and Ω do not exist at higher values of p and Ω. Furthermore, Figure 6 shows the effect of increasing the position-gain p and the rotor's eccentricity e on its amplitudes a_x and a_y at rotation speed $\Omega = 1.5$. Increasing the value of p is extremely important in this response curve because of the elimination of the unstable dashed branches that in turn eliminate the amplitude jumps with generated lower rotor's amplitudes, as shown. It is also appearing on the 3D surface that beyond the value $p = 1.4$, the rotor's amplitudes become linearly proportional of small slope with its eccentricity e. This can be illustrated from Eqs (8) and (9) where the cubic restoring force parameter $\varrho_1 = -6(p-1)(p-2)$. This parameter's value can mainly affect the nonlinear behavior of the curve (jump phenomenon and unstable branches). As can be noticed, if $p \to 2$, then the value of ϱ_1 approaches zero, which means the elimination of the curve's right-bending form.

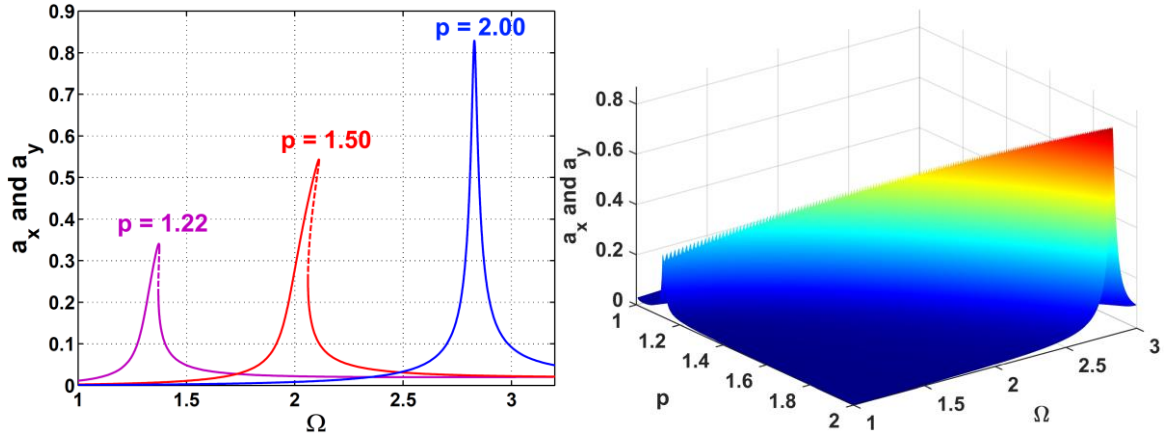

Figure 5. The rotor's amplitudes a_x and a_y vs. rotation speed Ω at different values of the position-gain p and eccentricity $e = 0.01$: (a) a_x and a_y vs. Ω, (b) 3D surface of a_x and a_y vs. Ω and p.

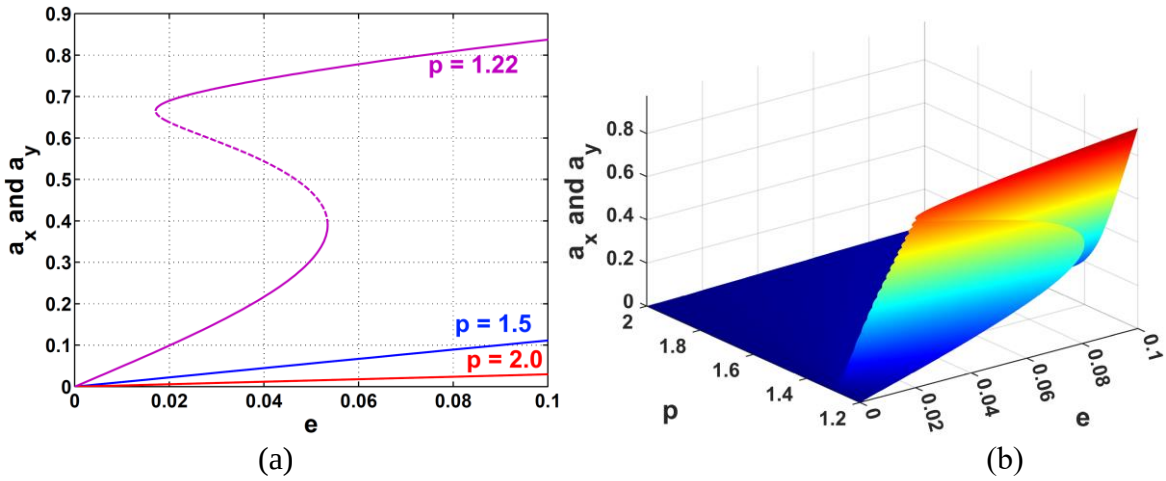

Figure 6. The rotor's amplitudes a_x and a_y vs. eccentricity e at different values of the position-gain p and rotation speed $\Omega = 1.5$: (a) a_x and a_y vs. e, (b) 3D surface of a_x and a_y vs. e and p.

As the effects of the position-gain p have been investigated on the rotor's amplitudes responses to its speed Ω and eccentricity e, the same analysis will be done with respect to the velocity-gain d. Figures 7 and 8 clarify such effects on the rotor's amplitudes at a position-gain value $p = 1.22$. The figures show that the velocity-gain d can enhance the damping performance of the rotor's oscillatory amplitudes. In Figure 7, the peak amplitudes have been suppressed monotonically with increasing d in addition to getting rid of the unstable dashed branches, as shown. Moreover, in Figure 8, raising d can eliminate the unstable dashed branches, too. This can be helpful in avoiding the amplitude jump either when varying the rotor's speed Ω or its eccentricity e.

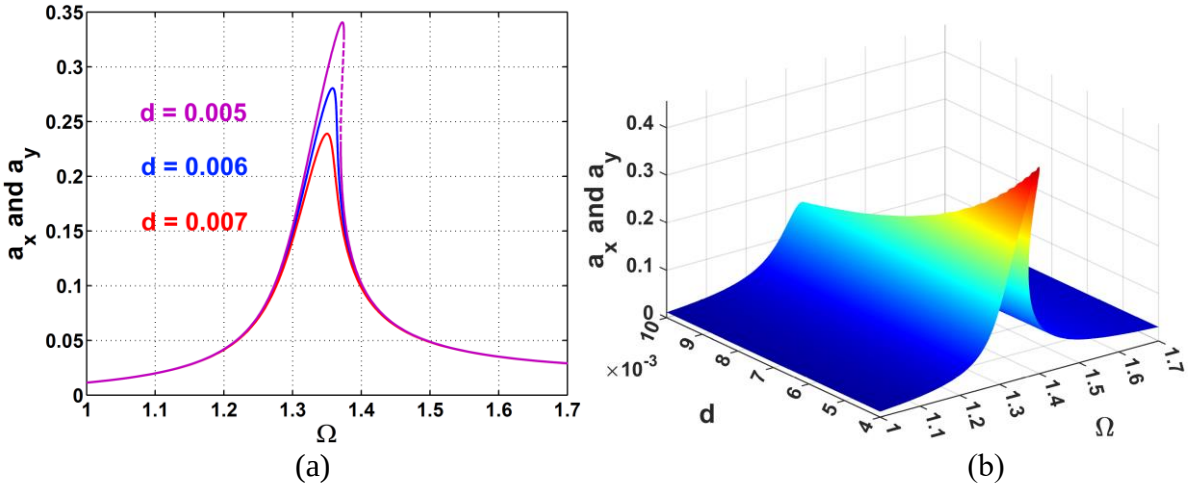

Figure 7. The rotor's amplitudes a_x and a_y vs. rotation speed Ω at different values of the velocity-gain d and eccentricity $e = 0.01$: (a) a_x and a_y vs. Ω, (b) 3D surface of a_x and a_y vs. Ω and d.

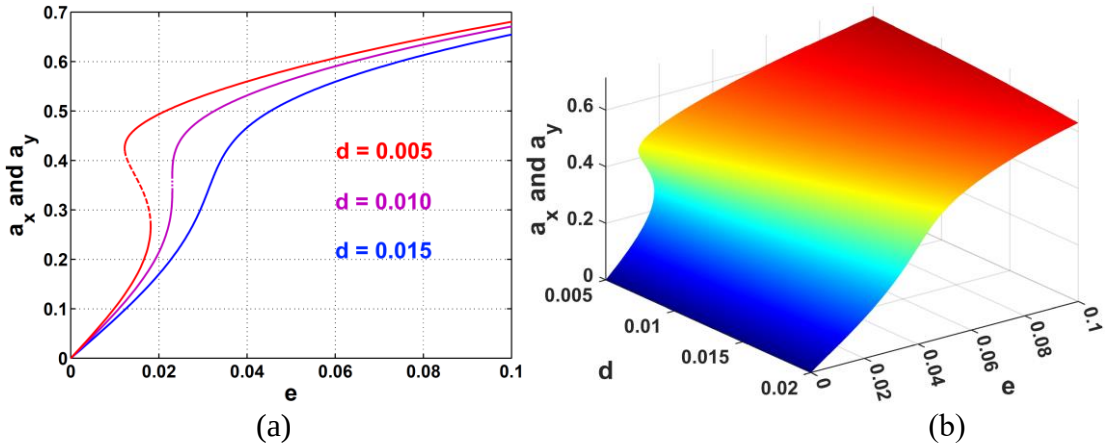

Figure 8. The rotor's amplitudes a_x and a_y vs. eccentricity e at different values of the velocity-gain d and rotation speed $\Omega = 1.4$: (a) a_x and a_y vs. e, (b) 3D surface of a_x and a_y vs. e and d.

3.2. Results on the relation between the configuration angle β and the Cartesian control scheme

Unlike the discussion in Section 3.1, the figures depending on the analysis done in Section 2.2 are plotted within this section. The damping factor ζ_c, the natural frequency ω_c, and the nonlinear coefficients η_1 to η_{15}, that are included in Eqs (25) and (26) are given in Appendix A as functions of the position-gain p, the velocity-gain d, and the configuration angle β. The plots of these coefficients in terms of β (in a range from $0°$ to $45°$) are included at fixed values of p and d to explore their dependence on β. Figure 9(a) shows the relation between ζ_c and β where it can reach its maximum value at $\beta = 22.5°$. This specific angle is where each pole is at the halfway point between its old position and the adjacent pole's old position. We can conclude that this Cartesian control method exhibits an optimum damping performance at $\beta = 22.5°$. Figure 9(b) pictures the relation between ω_c^2 and β where the maximum natural frequency happens also at $\beta = 22.5°$ and its minimum value occurs at $\beta = 0°$ (the initial or old pole's position in Figure 1(a)) or $\beta = 45°$ (the pole travels the

full way to take the adjacent pole's position). This preliminary discussion gives us a key that the configuration angle β affects the Cartesian control process severely.

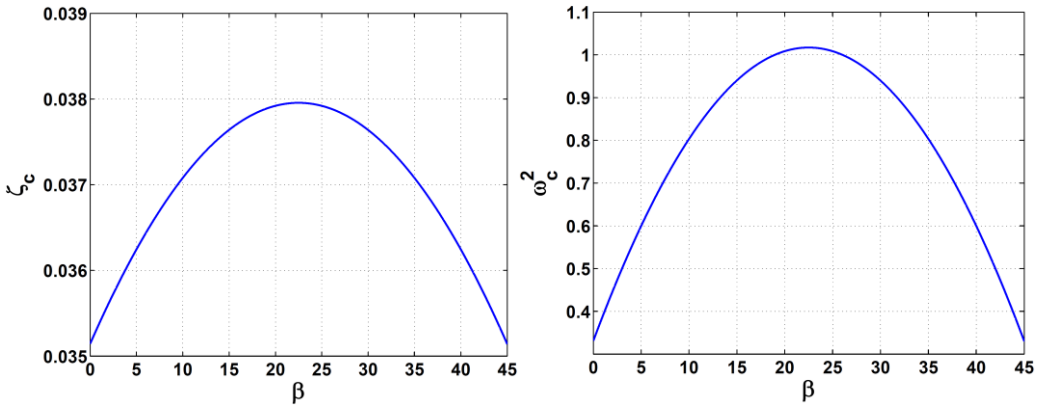

Figure 9. The relations between the damping ζ_c, the squared natural frequency ω_c^2 vs. the configuration angle β at $p = 1.22$ and $d = 0.005$: (a) ζ_c vs. β, (b) ω_c^2 vs. β.

The relations between the nonlinear coefficients η_1 (coefficient of x^3), η_2 (coefficient of xy^2), η_{10} (coefficient of x^2y), and η_{11} (coefficient of y^3) versus the configuration angle β are plotted in Figure 10. In Figure 10(a), we can see intersections between the curves of η_1 and η_2 at the angles $\beta = 5.3°$ and $\beta = 39.7°$ that will be discussed later. Also, the curve of η_1 has reached its maximum at the angle $\beta = 22.5°$, exactly where the curve of η_2 reached its minimum. On the other hand, in Figure 10(b), the values of η_{10} and η_{11} vanish simultaneously at the angle $\beta = 22.5°$.

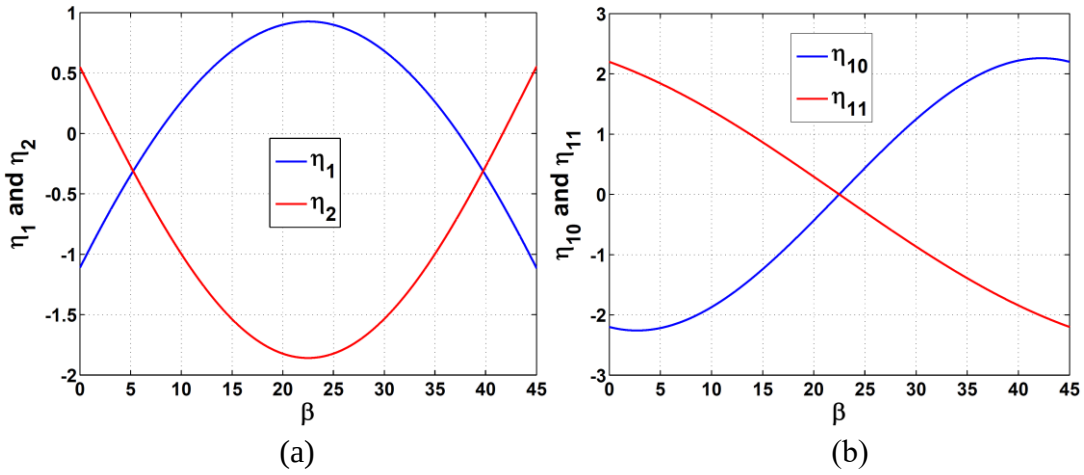

Figure 10. The relations between the nonlinear coefficients η_1, η_2, η_{10}, and η_{11} vs. the configuration angle β at $p = 1.22$ and $d = 0.005$: (a) η_1 and η_2 vs. β, (b) η_{10} and η_{11} vs. β.

Figure 11 pictures the nonlinear coefficients η_3 (coefficient of $x^2\dot{x}$), η_4 (coefficient of $\dot{x}y^2$), η_7 (coefficient of $xy\dot{y}$), η_{12} (coefficient of $x^2\dot{y}$), η_{13} (coefficient of $y^2\dot{y}$), and η_{15} (coefficient of $x\dot{x}y$) as functions of the configuration angle β. It can be noticed that the curves of η_4 and η_7 intersect at the angles $\beta = 8.3°$ and $\beta = 36.7°$. Accordingly, the curves of η_3 and η_4

have their maximum and minimum values at $\beta = 22.5°$. In Figure 11(b), the values of η_{12}, η_{13} and η_{15} reach the zero value at $\beta = 22.5°$.

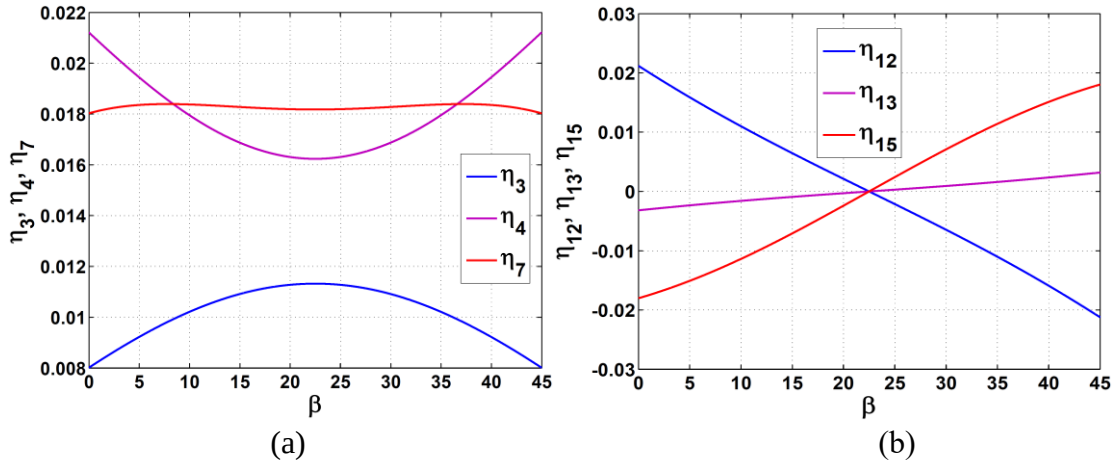

(a) (b)

Figure 11. The relations between the nonlinear coefficients η_3, η_4, η_7, η_{12}, η_{13}, and η_{15} vs. the configuration angle β at $p = 1.22$ and $d = 0.005$: (a) η_3, η_4 and η_7 vs. β, (b) η_{12}, η_{13} and η_{15} vs. β.

Figure 12 demonstrates how the nonlinear coefficients η_5 (coefficient of $x\dot{x}^2$), η_6 (coefficient of $x\dot{y}^2$), η_{14} (coefficient of $\dot{x}^2 y$ and $y\dot{y}^2$), η_8 (coefficient of $\dot{y}$), and η_9 (coefficient of y) are affected by varying the configuration angle β. At the angle $\beta = 22.5°$, the coefficients η_5 and η_6 become minimum and maximum, respectively. Moreover, the coefficients η_{14}, η_8 and η_9 are zeros at the same angle $\beta = 22.5°$ as shown.

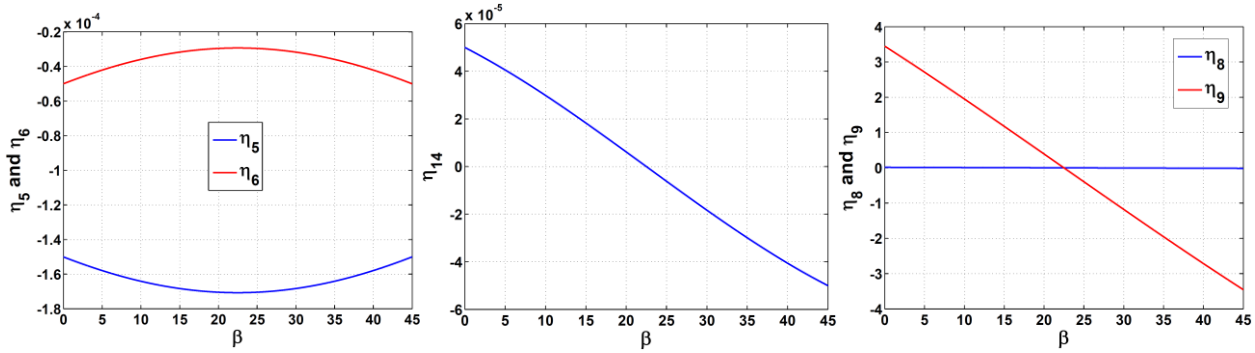

(a) (b) (c)

Figure 12. The relations between the nonlinear coefficients η_5, η_6, η_{14}, η_8, and η_9 vs. the configuration angle β at $p = 1.22$ and $d = 0.005$: (a) η_5 and η_6 vs. β, (b) η_{14} vs. β, (c) η_8 and η_9 vs. β.

In this control strategy, the rotor exhibits stable oscillations only at the configuration angle $\beta = 22.5°$ at which we introduce the following response curves based upon Eqs (27)–(30). The other responses, at different angles of β will be introduced later numerically. For the configuration angle $\beta = 22.5°$, the rotor's equilibrium amplitudes a_x and a_y have been plotted in response to the change of the rotor's rotation speed Ω at different values of its eccentricity e, as shown in Figure 13. It is noticeable that the rotor's amplitudes are high inside the band of rotor's speeds $\Omega \in [0.8, 1.2]$,

unlike the band of speeds that the radial-controlled rotor exhibited, i.e., $\Omega \in [1, 1.7]$. Moreover, as long as the rotor's eccentricity e increases, multiple stable solutions (up to three solid curves) can be noticed in Figure 13(c) in the band $\Omega \in [1.06, 1.18]$.

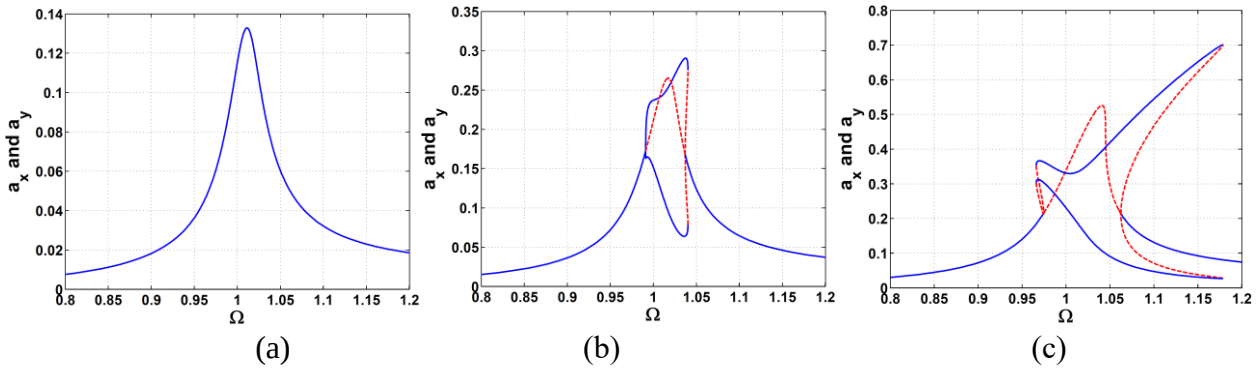

Figure 13. The rotor's amplitudes a_x and a_y vs. its rotation speed Ω at different values of its eccentricity e: (a) at $e = 0.005$, (b) at $e = 0.01$, (c) at $e = 0.02$.

Furthermore, at the same angle $\beta = 22.5°$, the rotor's equilibrium amplitudes a_x and a_y are depicted versus its eccentricity e at different values of its rotation speed Ω in Figure 14. The role of Ω is different from its role in the radial control case. Herein, the possibility of multiple solid curves existence accompanied by severe amplitude jumps can be noticed in the figure. In the case of $\Omega = 0.9$ (Figure 14(a)), three solid (stable) curves exist for $0.04 \leq e < 0.115$. At $e = 0.115$, the rotor passes through a Hopf bifurcation point at which there are two solid (stable) curves and one dashed (non-periodic unstable) curve. In the case of $\Omega = 1.0$ (Figure 14(b)), double solid curves appear only in the range $0.008 \leq e < 0.041$ after which the rotor passes through a Hopf bifurcation point. In the case of $\Omega = 1.1$ (Figure 14(c)), the most important issue that can be noticed is the rotor's impact with the stator pole legs at $e = 0.055$ where there are two other solid curves without the chance of such an impact.

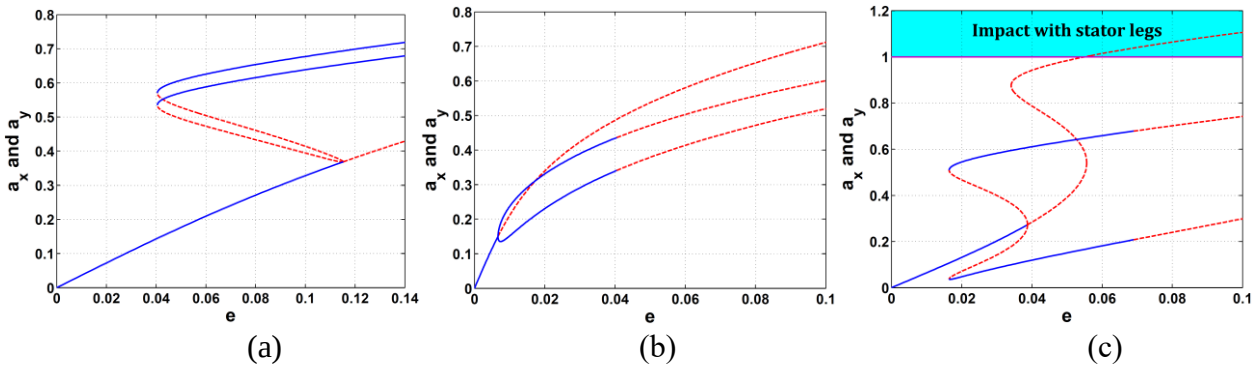

Figure 14. The rotor's amplitudes a_x and a_y vs. its eccentricity e at different values of its rotation speed Ω: (a) at $\Omega = 0.9$, (b) at $\Omega = 1.0$, (c) at $\Omega = 1.1$.

As discussed before in Figure 5, Figure 15 clarifies the influence of varying the position-gain p on the rotor's equilibrium amplitudes in response to its rotation speed Ω. Like Figure 5, the amplitudes increase with raising the value of p and the region of multiple solutions tends to vanish. There is still an issue in the shrunk region of multiple solutions that the number of solid curves increases to reach

up to four solid curves as shown in the close-up view in Figure 15(c). This will be verified numerically at a later stage. Accordingly, the effect of varying p on the amplitude-speed response curves is depicted in Figure 16. The responses in Figure 16(a) at $p = 1.22$ suffer from multiple stable solutions, then the amplitudes turn unstable beyond $e = 0.04$. On the other hand, raising the value of p can eliminate the solutions multiplicity in addition to smaller rotor's amplitudes in response to varying speed as shown in Figure 16(b),(c).

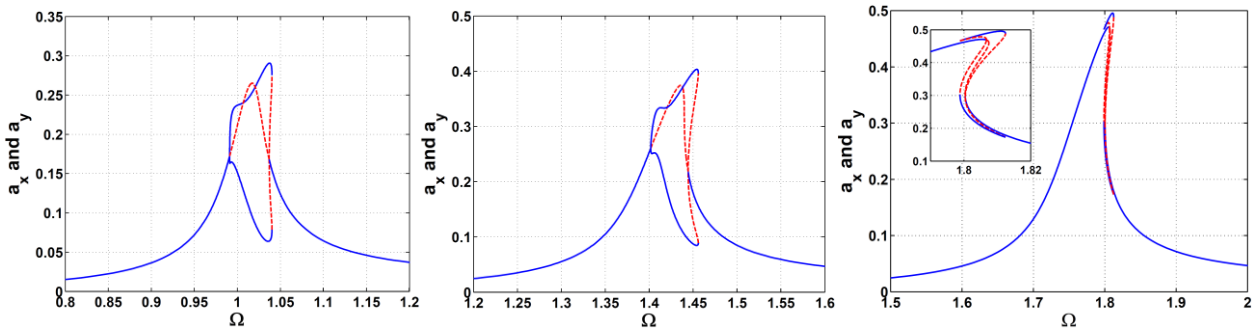

(a) (b) (c)

Figure 15. The rotor's amplitudes a_x and a_y vs. rotation speed Ω at different values of the position-gain p and eccentricity $e = 0.01$: (a) at $p = 1.22$, (b) at $p = 1.35$, (c) at $p = 1.50$.

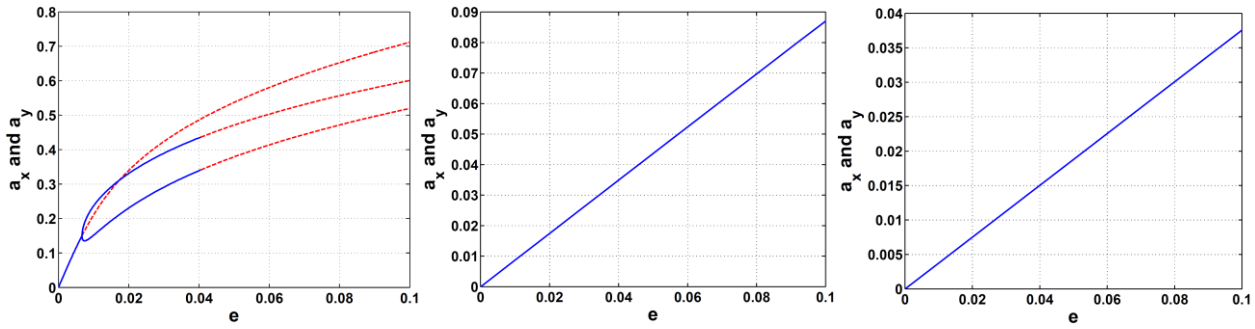

(a) (b) (c)

Figure 16. The rotor's amplitudes a_x and a_y vs. eccentricity e at different values of the position-gain p and rotation speed $\Omega = 1.00$: (a) at $p = 1.22$, (b) at $p = 1.35$, (c) at $p = 1.50$.

Similarly, Figures 17 and 18 show the effects of different values of the velocity-gain d on the rotor's amplitudes responses to its speed Ω (Figure 17) or to its eccentricity e (Figure 18) at $p = 1.22$. The parameter d guarantees a better damping performance for the rotor's operation. The reader can see that the amplitudes have been suppressed by increasing d and the region of multiple solutions shrinks as shown in Figure 17. In addition, the rotor's passage through Hopf points, in Figure 18(a) at $e = 0.04$, is delayed later when d increases as shown in Figure 18(b). In Figure 18(c), the Hopf points disappeared until the rotor's eccentricity reached $e = 0.1$, ensuring the important role of the velocity-gain d in the rotor's control process.

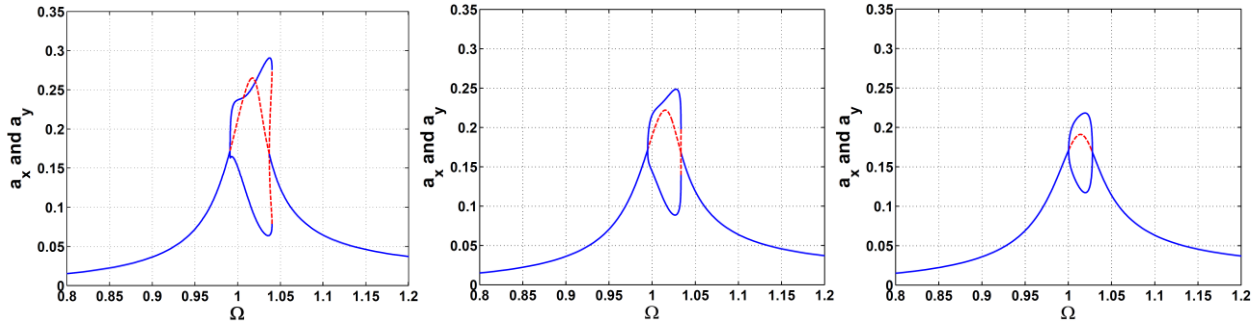

Figure 17. The rotor's amplitudes a_x and a_y vs. rotation speed Ω at different values of the velocity-gain d and eccentricity $e = 0.01$: (a) at $d = 0.005$, (b) at $d = 0.006$, (c) at $d = 0.007$.

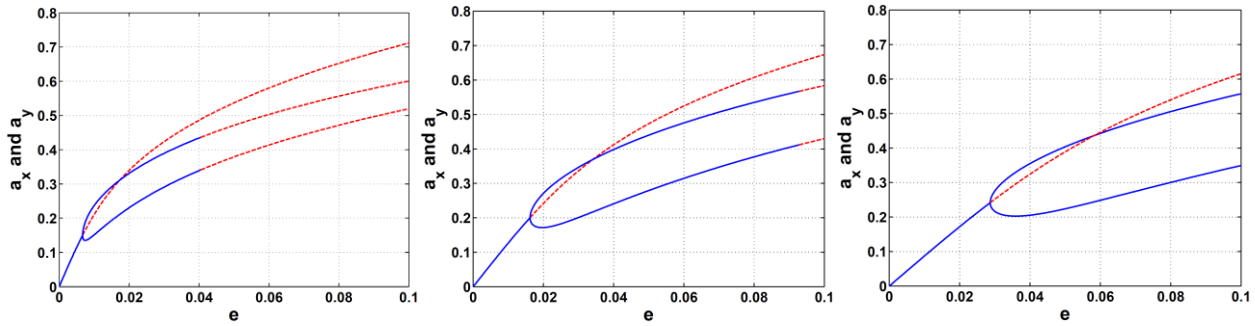

Figure 18. The rotor's amplitudes a_x and a_y vs. eccentricity e at different values of the velocity-gain d and rotation speed $\Omega = 1.00$: (a) at $d = 0.005$, (b) at $d = 0.010$, (c) at $d = 0.015$.

4. Numerical results and discussion

This section presents the simulation results upon direct integration of Eqs (8) and (9) for the radial control case, or Eqs (25) and (26) for the Cartesian control case. Different values of the configuration angle β have been adopted to show its effect on both control cases. The other adopted parameters will be used with the same values discussed in Section 3, $p = 1.22$, $d = 0.005$, $\delta_1 = 0.001$, $\Omega = 1.00$, and $e = 0.02$, unless otherwise mentioned. In the radial control scheme, we conclude that the configuration angle β does not affect the rotor's operation according to the invariant values of the nonlinear coefficients ϱ_1, ϱ_2, and ϱ_3. We are going to validate this behavior through the following figures. Figures 19–27 show the numerical simulation of the rotor's motion in the form of time responses, Poincare and orbit maps, and frequency spectra for both the horizontal and vertical displacements of the rotor. In Figures 19 and 20, these simulations display the effects of Ω's backward-sweeping and forward-sweeping on the rotor's oscillations amplitudes where there is a period-1 response with different amplitudes due to the sweeping process, as shown. The corresponding Poincare and orbit maps, in addition to the frequency spectra, have verified this period-1 response as shown in each figure. In the case that the position-gain p increases to $p = 2.00$, the period-1 response has not been changed but the rotor's critical speed moves to a bigger value $\Omega = 2.83$ as depicted in Figure 21.

Furthermore, the velocity-gain d can have a great damping influence on the rotor's amplitudes that were suppressed by about 70% if the value of d is raised from $d = 0.005$ to $d = 0.015$ as displayed in Figure 22. Figures 19–22 have been plotted at different values of the configuration angle β showing that it has no effect on the analytical or numerical responses in the case of radial control scheme, and the rotor exhibits symmetric oscillations for both $x(t)$ and $y(t)$ that are shown as circular orbits, as well.

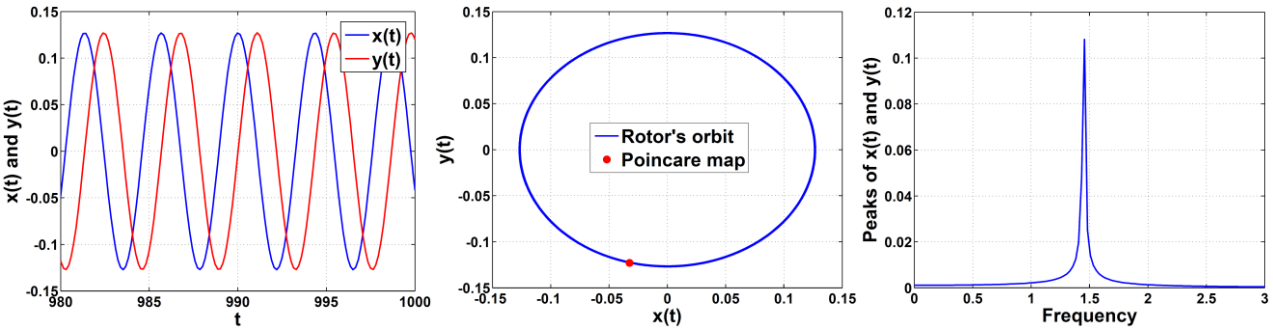

(a) (b) (c)

Figure 19. Simulation of rotor's backward-sweeping behavior of $x(t)$ and $y(t)$ in the case of radial control at $p = 1.22$, $d = 0.005$, $e = 0.02$, $\Omega = 1.45$, and different values of the angle β: (a) time response, (b) orbit and Poincare maps, (c) frequency spectra.

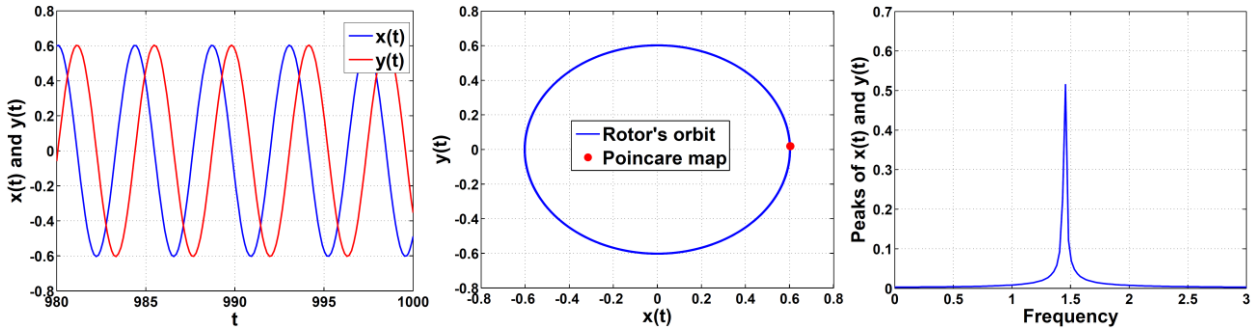

(a) (b) (c)

Figure 20. Simulation of rotor's forward-sweeping behavior of $x(t)$ and $y(t)$ in the case of radial control at $p = 1.22$, $d = 0.005$, $e = 0.02$, $\Omega = 1.45$, and different values of the angle β: (a) time response, (b) orbit and Poincare maps, (c) frequency spectra.

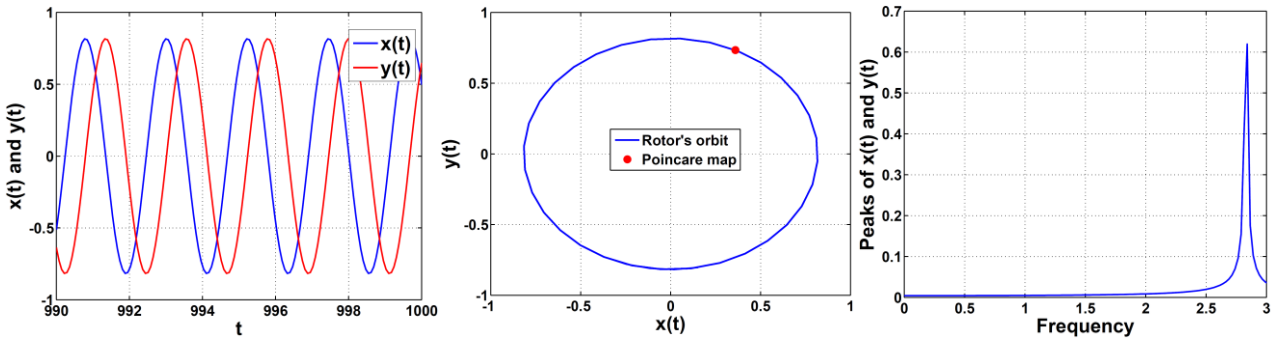

(a) (b) (c)

Figure 21. Simulation of rotor's behavior of $x(t)$ and $y(t)$ in the case of radial control at $p = 2.00$, $d = 0.005$, $e = 0.01$, $\Omega = 2.83$, and different values of the angle β: (a) time response, (b) orbit and Poincare maps, (c) frequency spectra.

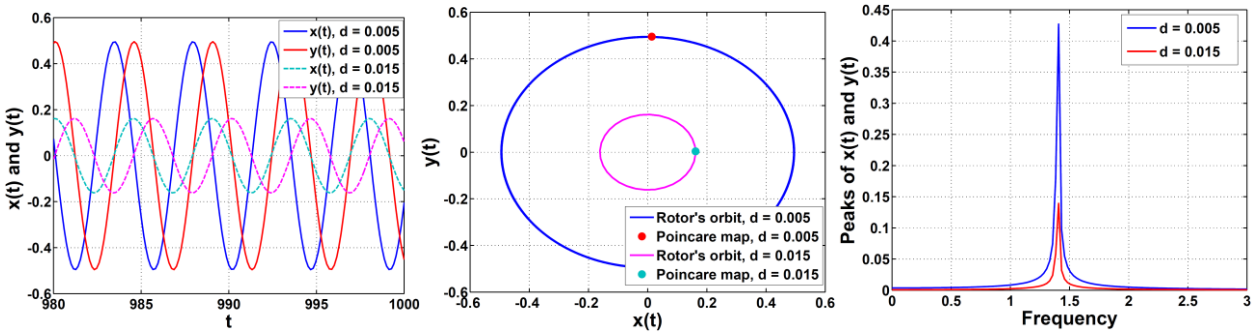

(a) (b) (c)

Figure 22. Simulation of rotor's behavior of $x(t)$ and $y(t)$ in the case of radial control at $p = 1.22$, $d = \{0.005, 0.015\}$, $e = 0.02$, $\Omega = 1.4$, and different values of the angle β: (a) time response, (b) orbit and Poincare maps, (c) frequency spectra.

In the case of a Cartesian control scheme, Figures 23–28 clarify the simulation of the rotor's oscillations in response to varying its eccentricity e and at a configuration angle $\beta = 22.5°$. In Figure 23, there exists a period-1 response, which is verified by the corresponding Poincare and orbit maps as well as the frequency spectra. Unlike the radial control scheme, the rotor exhibits asymmetric oscillations for both $x(t)$ and $y(t)$ that are shown as elliptic orbits. If the rotor's eccentricity is raised to $e = 0.04$, as in Figure 24, a quasiperiodic response is approached where the Poincare map is a closed trajectory or pattern as displayed. By raising e to 0.059, the rotor follows a multi-periodic (period-9) response as depicted by the Poincare map in Figure 25. At $e = 0.06$ in Figure 26, a hybrid response between quasiperiodic and chaotic happens where the Poincare map depicts a closed pattern with discrete dots as shown. Figure 27 shows the rotor's chaotic behavior when its eccentricity reaches $e = 0.08$. The Poincare section now is a form of scattered dots without any pattern and, correspondingly, the frequency spectra contain a big number of spikes denoting chaos. Accordingly, Figure 28 clarifies the bifurcation diagram of the rotor's motion in response to its varying eccentricity e.

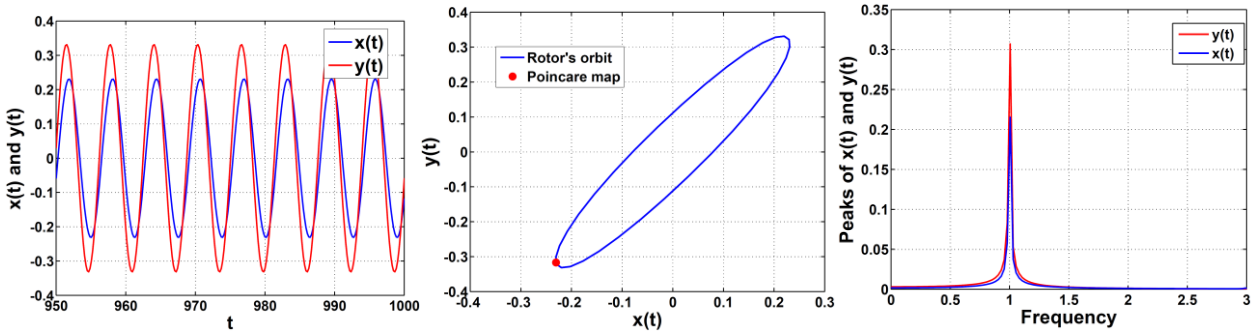

(a) (b) (c)

Figure 23. Simulation of rotor's behavior of $x(t)$ and $y(t)$ in the case of Cartesian control at $p = 1.22$, $d = 0.005$, $e = 0.02$, $\Omega = 1.00$, and $\beta = 22.5°$: (a) time response, (b) orbit and Poincare maps, (c) frequency spectra.

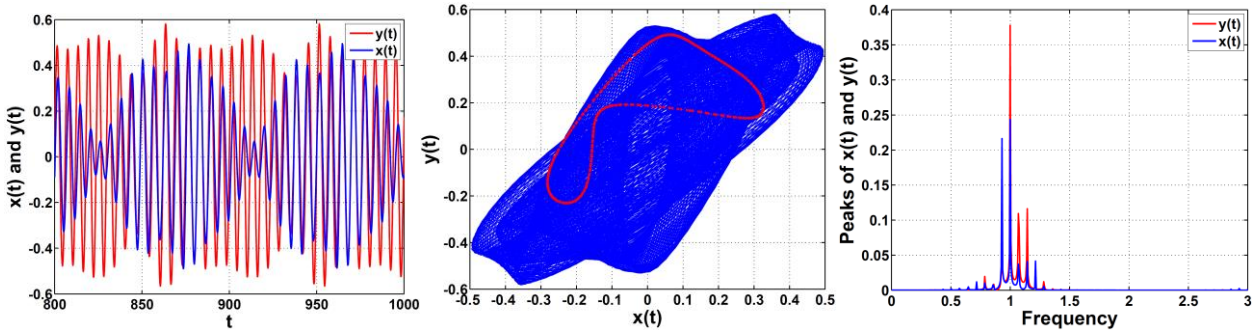

(a) (b) (c)

Figure 24. Simulation of rotor's behavior of $x(t)$ and $y(t)$ in the case of Cartesian control at $p = 1.22$, $d = 0.005$, $e = 0.04$, $\Omega = 1.00$, and $\beta = 22.5°$: (a) time response, (b) orbit and Poincare maps, (c) frequency spectra.

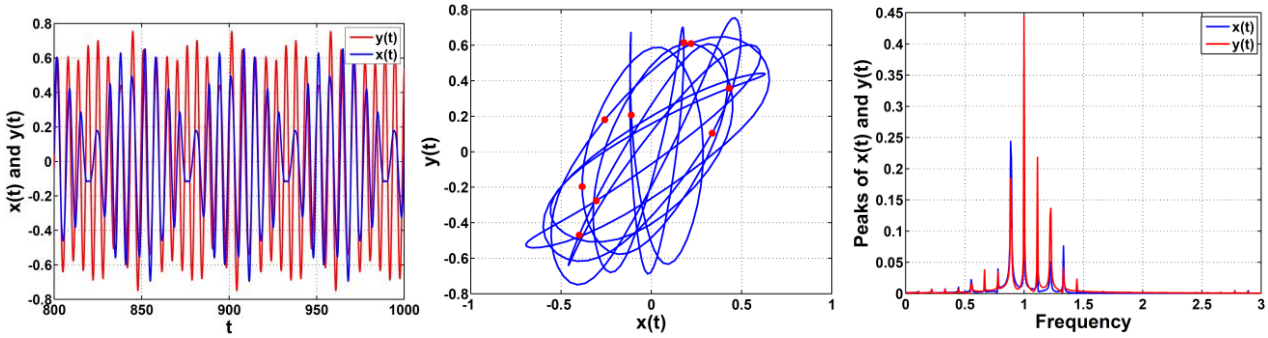

(a) (b) (c)

Figure 25. Simulation of rotor's behavior of $x(t)$ and $y(t)$ in the case of Cartesian control at $p = 1.22$, $d = 0.005$, $e = 0.059$, $\Omega = 1.00$, and $\beta = 22.5°$: (a) time response, (b) orbit and Poincare maps, (c) frequency spectra.

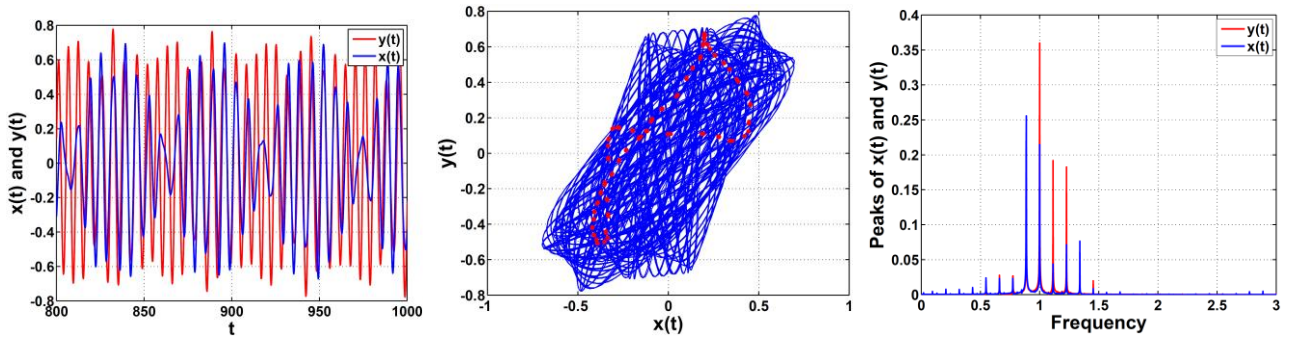

(a) (b) (c)

Figure 26. Simulation of rotor's behavior of $x(t)$ and $y(t)$ in the case of Cartesian control at $p = 1.22$, $d = 0.005$, $e = 0.06$, $\Omega = 1.00$, and $\beta = 22.5°$: (a) time response, (b) orbit and Poincare maps, (c) frequency spectra.

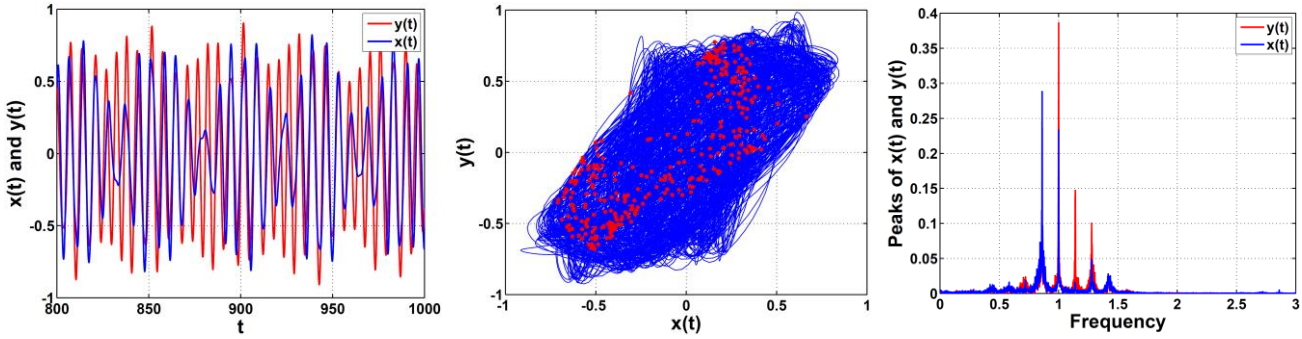

(a) (b) (c)

Figure 27. Simulation of rotor's behavior of $x(t)$ and $y(t)$ in the case of Cartesian control at $p = 1.22$, $d = 0.005$, $e = 0.08$, $\Omega = 1.00$, and $\beta = 22.5°$: (a) time response, (b) orbit and Poincare maps, (c) frequency spectra.

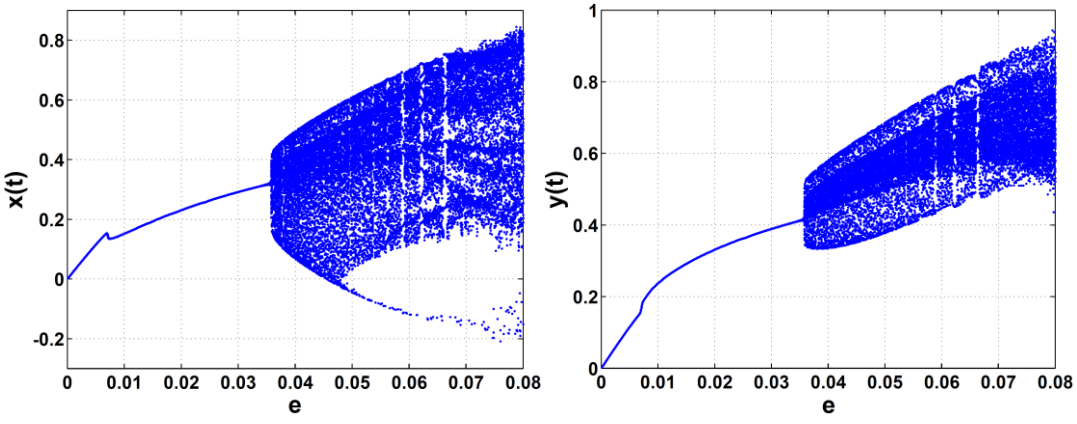

(a) (b)

Figure 28. Rotor's bifurcation behavior in response to its eccentricity e in the case of Cartesian control at $p = 1.22$, $d = 0.005$, $\Omega = 1.00$, and $\beta = 22.5°$: (a) $x(t)$ vs. e, (b) $y(t)$ vs. e.

The effect of varying the configuration angle β on the rotor's oscillations in the case of the Cartesian control method is discussed in Figures 29 and 30. In these two figures, we have plotted $x(t)$ and $y(t)$ as functions of time and, upon them, the radial displacement $r(t) = \sqrt{[x(t)]^2 + [y(t)]^2}$ is also plotted to see when the rotor is impacting with the stator legs. In Figure 29, the configuration angle β is varied from its initial value $\beta = 0°$ to $\beta = 20°$. As can be seen, the rotor impacts with the stator legs at $t \approx 4.1$ and $\beta = 0°$, while the possibility of impact is deferred if the configuration angle β increases just before the optimum angle $\beta = 22.5°$. This optimum angle has been proven to make the rotor work safely with poor possibility of impact. Afterward, the angle has been raised to $\beta = 25°$ and the rotor starts to hit the stator at $t \approx 8$. If the angle is raised more and more away from the optimum one ($\beta = 22.5°$), the impact possibility becomes faster in time, as shown.

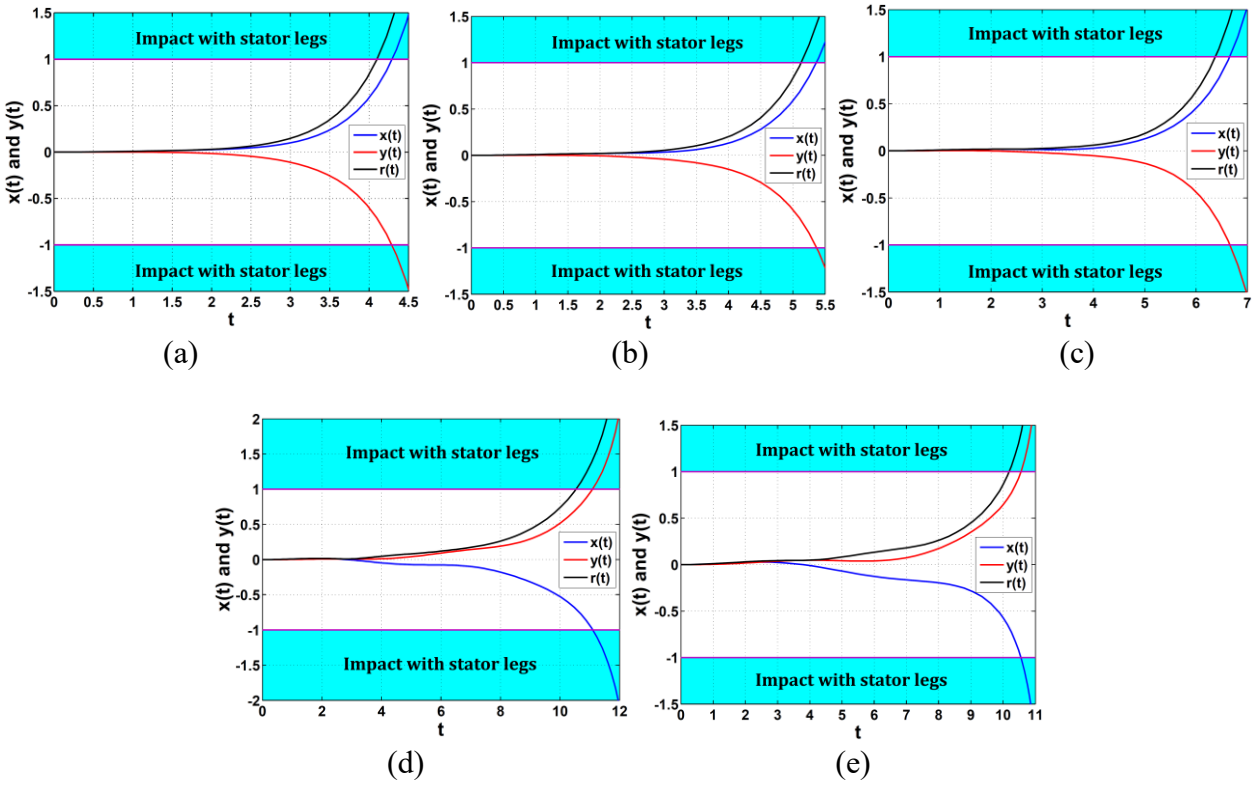

Figure 29. Effects of varying the configuration angle β on the temporal oscillations of the rotor in the case of Cartesian control at $p = 1.22$, $d = 0.005$, $e = 0.02$, and $\Omega = 1.00$: (a) $\beta = 0°$, (b) $\beta = 5.3°$, (c) $\beta = 8.3°$, (d) $\beta = 15°$, (e) $\beta = 20°$.

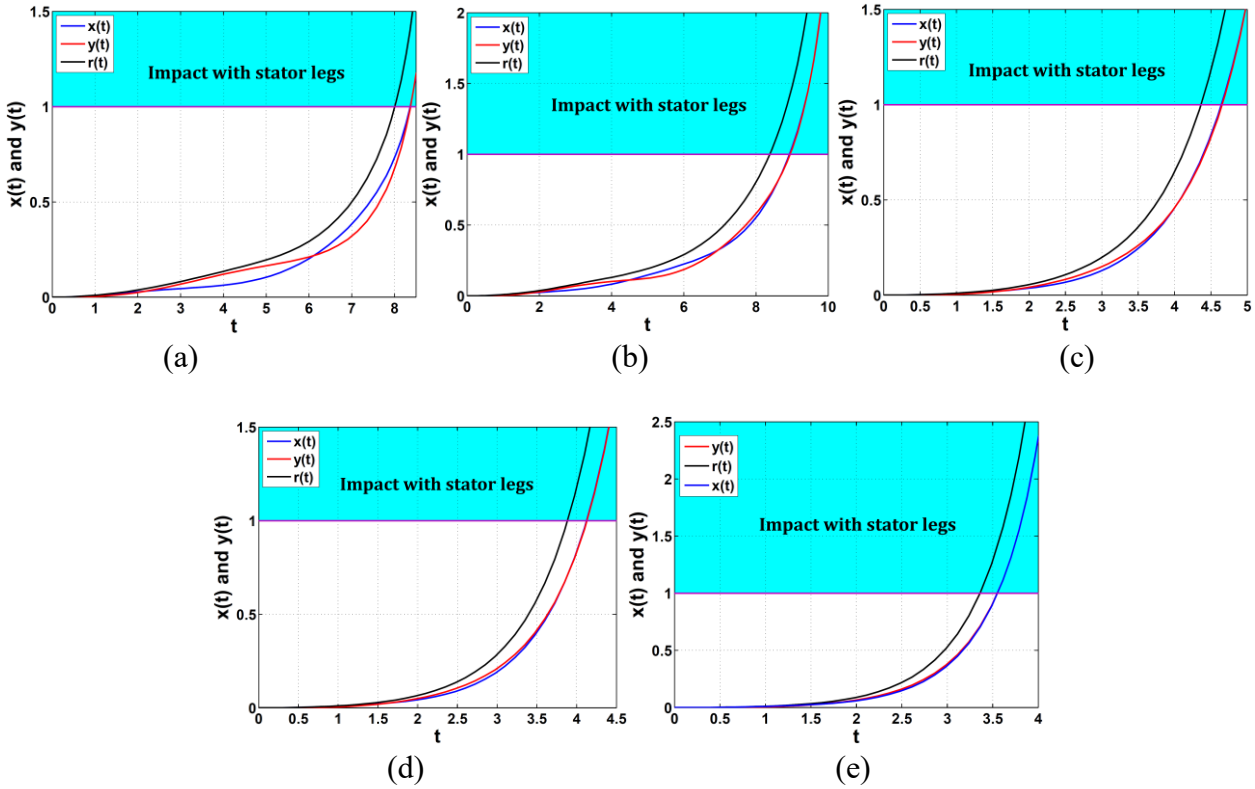

Figure 30. Effects of varying the configuration angle β on the temporal oscillations of the rotor in the case of Cartesian control at $p = 1.22$, $d = 0.005$, $e = 0.02$, and $\Omega = 1.00$: (a) $\beta = 25°$, (b) $\beta = 30°$, (c) $\beta = 36.7°$, (d) $\beta = 39.7°$, (e) $\beta = 45°$.

5. Conclusions

This work focused on the effect of the configuration angle on the control process of an oscillatory rotor in 8-pole active magnetic bearings. The mentioned angle is between the axis of a specific pair of poles and the positive x-axis. Adopting the PD control algorithm, the well-known radial control and Cartesian control techniques were applied in this work. The approximate modulating amplitudes and phases of the rotor's oscillations were extracted by the method of multiple-scales and a stability condition was built based on testing the corresponding Jacobian matrix. This study can be summarized in the following notes. In the radial control scheme, the rotor's equilibrium amplitudes were not affected by the change in the configuration angle, even if the rotor's rotation speed Ω and eccentricity e were varied. The rotor's numerical responses exhibited symmetric and periodic (period-1) oscillations that were shown as circular orbits at different adopted values of the configuration angle.

In the Cartesian control scheme, the damping parameter ζ_c could reach its maximum value (optimum damping performance) at a configuration angle $\beta = 22.5°$. In addition, the rotor's motion natural frequency was also affected by the change in the configuration angle where it was also maximum at $\beta = 22.5°$. At such an angle, different responses (periodic, multi-periodic, quasiperiodic, and chaotic) were shown when the rotor's eccentricity increased. Eventually, different configuration angles ($\beta \neq 22.5°$) were affecting the rotor's oscillations severely where the rotor impacted with the stator legs in small intervals of time.

Use of AI tools declaration

The authors declare that they have not used artificial intelligence (AI) tools in the creation of this article.

Acknowledgments

The authors extend their appreciation to King Saud University, Saudi Arabia, for funding this work through Researchers Supporting Project number (RSPD2024R704), King Saud University, Riyadh, Saudi Arabia. The authors are also very grateful for the financial support from the National Key Research and Development Program of China (Grant No. 2023YFE0125900).

Conflict of interest

The authors declare no potential conflicts of interest with respect to the research, authorship, and/or publication of this article.

References

1. J. C. Ji, C. H. Hansen, Non-linear oscillations of a rotor in active magnetic bearings, *J. Sound Vib.*, **240** (2001), 599–612. https://doi.org/10.1006/jsvi.2000.3257
2. J. C. Ji, Dynamics of a Jeffcott rotor-magnetic bearing system with time delays, *Int. J. Non. Linear. Mech.*, **38** (2003), 1387–1401. https://doi.org/10.1016/S0020-7462(02)00078-1
3. W. Zhang, X. P. Zhan, Periodic and chaotic motions of a rotor-active magnetic bearing with quadratic and cubic terms and time-varying stiffness, *Nonlinear Dyn.*, **41** (2005), 331–359. https://doi.org/10.1007/s11071-005-7959-2
4. X. Y. Li, Y. S. Chen, Z. Q. Wu, T. Song, Response of parametrically excited Duffing-van der Pol oscillator with delayed feedback, *Appl. Math. Mech.*, **27** (2006), 1585–1595. https://doi.org/10.1007/s10483-006-1201-z
5. P. Y. Couzon, J. Der Hagopian, Neuro-fuzzy active control of rotor suspended on active magnetic bearing, *J. Vib. Control*, **13** (2007), 365–384. https://doi.org/10.1177/1077546307074578
6. J. C. Ji, C. H. Hansen, A. C. Zander, Nonlinear dynamics of magnetic bearing systems, *J. Intel. Mat. Syst. Str.*, **19** (2008), 1471–1491. https://doi.org/10.1177/1045389X08088666
7. T. Inoue, Y. Sugawara, Nonlinear vibration analysis of a rigid rotating shaft supported by the magnetic bearing (influence of the integral feedback in the PID control of the vertical shaft), *J. Syst. Des. Dyn.,* **4** (2010), 471–483. https://doi.org/10.1299/jsdd.4.471
8. T. Inoue, Y. Sugawara, M. Sugiyama, Modeling and nonlinear vibration analysis of a rigid rotor system supported by the magnetic bearing (effects of delays of both electric current and magnetic flux), *J. Appl. Mech.-T. ASME.*, **77** (2010), 1–10. https://doi.org/10.1115/1.3172139
9. M. Eissa, M. Kamel, H. S. Bauomy, Nonlinear behavior of tuned rotor-AMB system with time varying stiffness, *Int. J. Bifurcat. Chaos*, **21** (2011), 195–207. https://doi.org/10.1142/S0218127411028362
10. X. Y. Xu, W. H: Jiang, Singularity analysis of Jeffcott rotor-magnetic bearing with time delays, *Appl. Math.*, **27** (2012), 419–427. https://doi.org/10.1007/s11766-012-2752-8
11. L. Li, Y. J. Han, Z. Y. Ren, Nonlinear study of rotor-AMB system subject to multi-parametric excitations, *Appl. Mech. Mater.*, **397** (2013), 359–364. https://doi.org/10.4028/www.scientific.net/AMM.397-400.359

12. X. D. Yang, H. Z. An, Y. J. Qian, W. Zhang, M. H. Yao, Elliptic motions and control of rotors suspending in active magnetic bearings, *J. Comput. Nonlinear Dyn.*, **11** (2016), 1–8. https://doi.org/10.1115/1.4033659
13. R. Ebrahimi, M. Ghayour, H. M. Khanlo, Chaotic vibration analysis of a coaxial rotor system in active magnetic bearings and contact with auxiliary bearings, *J. Comput. Nonlinear Dyn.*, **12** (2017). https://doi.org/10.1115/1.4034869
14. R. Q. Wu, W. Zhang, M. H. Yao, Nonlinear dynamics near resonances of a rotor-active magnetic bearings system with 16-pole legs and time varying stiffness, *Mech. Syst. Signal Pr.*, **100** (2018), 113–134. https://doi.org/10.1016/j.ymssp.2017.07.033
15. A. K. Jha, S. S. Dasgupta, Attenuation of Sommerfeld effect in an internally damped eccentric shaft-disk system via active magnetic bearings, *Meccanica*, **54** (2019), 311–320. https://doi.org/10.1007/s11012-018-00936-7
16. Z. Sun, X. Zhang, T. Fan, X. Yan, J. Zhao, L. Zhao, et al., Nonlinear dynamic characteristics analysis of active magnetic bearing system based on cell mapping method with a case study, *Mech. Syst. Signal Pr.*, **117** (2019), 116–137. https://doi.org/10.1016/j.ymssp.2018.07.030
17. N. A. Saeed, A. Kandil, Lateral vibration control and stabilization of the quasiperiodic oscillations for rotor-active magnetic bearings system, *Nonlinear Dyn.*, **98** (2019), 1191–1218. https://doi.org/10.1007/s11071-019-05256-3
18. S. A. A. Hosseini, A. Yektanezhad, Primary resonance analysis of a nonlinear flexible shaft supported by active magnetic bearings using analytical method, *ZAMM-Z. Angew. Math. Me.*, **100** (2020). https://doi.org/10.1002/zamm.201900145
19. A. Kandil, M. Sayed, N. A. Saeed, On the nonlinear dynamics of constant stiffness coefficients 16-pole rotor active magnetic bearings system, *Eur. J. Mech. A-Solid.*, **84** (2020), 104051. https://doi.org/10.1016/j.euromechsol.2020.104051
20. A. Kandil, Investigation of the whirling motion and rub/impact occurrence in a 16-pole rotor active magnetic bearings system with constant stiffness, *Nonlinear Dynam.*, **102** (2020), 2247–2265. https://doi.org/10.1007/s11071-020-06071-x
21. W. S. Ma, W. Zhang, Y. F. Zhang, Stability and multi-pulse jumping chaotic vibrations of a rotor-active magnetic bearing system with 16-pole legs under mechanical-electric-electromagnetic excitations, *Eur. J. Mech. A-Solids.*, **85** (2021). https://doi.org/10.1016/j.euromechsol.2020.104120
22. A. Kandil, Y. S. Hamed, Tuned positive position feedback control of an active magnetic bearings system with 16-Poles and constant stiffness, *IEEE Access*, **9** (2021), 73857–73872. https://doi.org/10.1109/ACCESS.2021.3080457
23. S. Zhong, L. Li, H. Chen, Z. Lu, A novel balancing method for rotor using unsupervised deep learning, *Shock Vib.*, **2021** (2021). https://doi.org/10.1155/2021/1800164
24. A. Kandil, Y. S. Hamed, A. M. Alsharif, Rotor active magnetic bearings system control via a tuned nonlinear saturation oscillator, *IEEE Access*, **9** (2021), 133694–133709. https://doi.org/10.1109/ACCESS.2021.3114356
25. N. A. Saeed, A. Kandil, Two different control strategies for 16-pole rotor active magnetic bearings system with constant stiffness coefficients, *Appl. Math. Model.*, **92** (2021), 1–22. https://doi.org/10.1016/j.apm.2020.11.005
26. G. Zhang, G. Xi, Vibration control of a time-delayed rotor-active magnetic bearing system by time-varying stiffness, *Int. J. Appl. Mech.*, **14** (2022). https://doi.org/10.1142/S1758825122500077
27. T. Du, H. Geng, B. Wang, H. Lin, L. Yu, Nonlinear oscillation of active magnetic bearing-rotor systems with a time-delayed proportional-derivative controller, *Nonlinear Dynam.*, **109** (2022), 2499–2523. https://doi.org/10.1007/s11071-022-07557-6

28. G. Zhang, P. Zhang, Z. Wang, G. Xi, H. Zou, Nonlinear vibration of a magnetic bearing-rotor system based on PD control, *Journal Vib. Shock.*, **41** (2022), 99–105. https://doi.org/10.13465/j.cnki.jvs.2022.10.013
29. T. Yu, Z. Zhang, Y. Li, W. Zhao, J. Zhang, Improved active disturbance rejection controller for rotor system of magnetic levitation turbomachinery, *Electron. Res. Arch.*, **31** (2023), 1570–1586. https://doi.org/10.3934/ERA.2023080
30. P. K. Meher, M. A. Ansari, A. Bisoi, Effect of bias current of active magnetic bearing on Sommerfeld effect characterization in an unbalanced rotor dynamic system, *Acta Mech.*, **235** (2024), 907–923. https://doi.org/10.1007/s00707-023-03772-3
31. W. S. Takam, A. M. Kongne, D. Yemélé, Nonlinear dynamics of two dimensional rotor-active magnetic bearing system with generalized-pole legs: stability state diagram and control strategy, *Nonlinear Dynam.*, **111** (2023), 17909–17937. https://doi.org/10.1007/s11071-023-08800-4
32. W. Zhang, M. H. Yao, X. P. Zhan, Multi-pulse chaotic motions of a rotor-active magnetic bearing system with time-varying stiffness, *Chaos Soliton. Fract.*, **27** (2006), 175–186. https://doi.org/10.1016/j.chaos.2005.04.003
33. J. Li, Y. Tian, W. Zhang, S. F. Miao, Bifurcation of multiple limit cycles for a rotor-active magnetic bearings system with time-varying stiffness, *Int. J. Bifurc. Chaos*, **18** (2008), 755–778. https://doi.org/10.1142/S021812740802063X
34. W. Zhang, J. W. Zu, Transient and steady nonlinear responses for a rotor-active magnetic bearings system with time-varying stiffness, *Chaos Soliton. Fract.*, **38** (2008), 1152–1167. https://doi.org/10.1016/j.chaos.2007.02.002
35. W. Zhang, J. W. Zu, F. X. Wang, Global bifurcations and chaos for a rotor-active magnetic bearing system with time-varying stiffness, *Chaos Soliton. Fract.*, **35** (2008), 586–608. https://doi.org/10.1016/j.chaos.2006.05.095
36. W. Zhang, R. Q. Wu, B. Siriguleng, Nonlinear vibrations of a rotor-active magnetic bearing system with 16-Pole legs and two degrees of freedom, *Shock Vib.*, **2020** (2020), 5282904. https://doi.org/10.1155/2020/5282904
37. B. Yang, C. Peng, F. Jiang, S. Shi, A novel model calibration method for active magnetic bearing based on deep reinforcement learning, *Guid. Navig. Control*, **3** (2023), 2350017. https://doi.org/10.1142/S2737480723500176
38. X. Xu, Y. Liu, Q. Han, A universal dynamic model and solution scheme for the electrical rotor system with wide range of eccentricity, *Int. J. Nonlinear. Mech.*, **152** (2023), 104402. https://doi.org/10.1016/j.ijnonlinmec.2023.104402
39. S. Wei, J. Zhou, X. Han, S. Zheng, A simplified analysis method and suppression of the modalities of a magnetic levitation turbo rotor system, *Vacuum.*, **217** (2023), 112452. https://doi.org/10.1016/j.vacuum.2023.112452
40. F. Y. Saket, P. S. Keogh, Force-based feedforward control of persistent synchronous rotor/touchdown bearing contact in active magnetic bearing systems, *Mech. Syst. Signal Pr.*, **201** (2023), 110657. https://doi.org/10.1016/j.ymssp.2023.110657
41. Q. Liu, L. Wang, M. Feng, Clearance compatibility and design principle of the single-structured hybrid gas-magnetic bearing, *Ind. Lubr. Tribol.*, **75** (2023), 1219–1228. https://doi.org/10.1108/ILT-03-2023-0077
42. S. Wei, Y. Le, J. Zhou, Y. Yin, D. Zhang, S. Zheng, Stability control of high-speed magnetic levitation turbomolecular pumps with shock-excited disturbance, *ISA T.*, **142** (2023), 585–593. https://doi.org/10.1016/j.isatra.2023.07.045

43. P. Jiang, Y. Tian, B. Wang, C. Guo, Design and analysis of centrifugal compressor in carbon dioxide heat pump system, *Sci. Rep.*, **14** (2024), 5286. https://doi.org/10.1038/s41598-024-55698-y
44. J. Han, Y. Li, F. Xiong, Y. Zuo, N. Zhang, Study on modeling and analysis method of active magnetic bearing-flexible support coupled system, *J. Vib. Eng. Technol.*, **12** (2024), 995–1006. https://doi.org/10.1007/s42417-023-00889-6
45. Y. Ishida, T. Yamamoto, *Linear and nonlinear rotor dynamics: A modern treatment with applications*, 2 Eds., Wiley-VCH Verlag GmbH & Co. KGaA, 2012. https://doi.org/10.1002/9783527651894
46. A. H. Nayfeh, D. T. Mook, *Nonlinear oscillations*, Wiley-VCH Verlag GmbH & Co. KGaA, 1995. https://doi.org/10.1002/9783527617586

Appendix

Appendix A

The parameters of Eqs (8) and (9):

$$p = I_0 C_0 g_1,$$

$$d = \frac{I_0 C_0 g_2}{B},$$

$$\delta_1 = \frac{B\delta}{M},$$

$$\zeta_r = \delta_1 + 8d,$$

$$e = \frac{E}{C_0},$$

$$\omega_r^2 = 8(p-1),$$

$$\begin{aligned}\varrho_1 = {} & -16 + 24p - 24\cos^2\beta\sin^2\beta - 2p^2\sin^4\beta + 16\cos\beta\sin^3\beta - 16\sin\beta\cos\beta \\ & + 16\sin\beta\cos^3\beta + 12p^2\cos^2\beta - 10p^2\cos^4\beta + 30p\cos^4\beta + 6p\sin^4\beta \\ & + 4p^2\sin^2\beta - 36p\cos^2\beta - 12p\sin^2\beta + 36p\cos^2\beta\sin^2\beta + 24p\sin\beta\cos\beta \\ & - 12p^2\cos^2\beta\sin^2\beta - 24p\sin\beta\cos^3\beta - 24p\cos\beta\sin^3\beta + 8p^2\sin\beta\cos^3\beta \\ & - 8p^2\sin\beta\cos\beta + 8p^2\cos\beta\sin^3\beta + 8\sin^2\beta - 8p^2 - 4\sin^4\beta - 20\cos^4\beta \\ & + 24\cos^2\beta,\end{aligned}$$

$$\begin{aligned}\varrho_2 = {} & -24d\sin\beta\cos\beta + 20dp\cos^4\beta - 36d\cos^2\beta\sin^2\beta + 4dp\sin^4\beta - 24dp\cos^2\beta \\ & + 16dp\sin\beta\cos\beta - 6d\sin^4\beta - 8dp\sin^2\beta + 24d\cos\beta\sin^3\beta - 30d\cos^4\beta \\ & + 24dp\cos^2\beta\sin^2\beta + 36d\cos^2\beta + 12d\sin^2\beta - 16dp\cos\beta\sin^3\beta \\ & - 16dp\sin\beta\cos^3\beta + 24d\sin\beta\cos^3\beta,\end{aligned}$$

$$\begin{aligned}\varrho_3 = {} & 10d^2\cos^4\beta - 4d^2\sin^2\beta - 12d^2\cos^2\beta + 2d^2\sin^4\beta + 12d^2\cos^2\beta\sin^2\beta \\ & - 8d^2\cos\beta\sin^3\beta + 8d^2\sin\beta\cos\beta - 8d^2\sin\beta\cos^3\beta.\end{aligned}$$

The parameters of Eqs (25) and (26):

$$\zeta_c = 2\sqrt{2}d\left(\left(1+\sqrt{2}\right)\cos\beta + \sin\beta\right) + \delta_1,$$

$$\omega_c^2 = 2\sqrt{2}p\left(\left(1+\sqrt{2}\right)\cos\beta + \sin\beta\right) - 8,$$

$$\eta_1 = -\frac{3p}{\sqrt{2}}\left(\left(1-\sqrt{2}\right)\cos(3\beta) - \sin(3\beta)\right) - 2p^2(\cos(2\beta) + \sin(2\beta) + 2) + \frac{9p}{\sqrt{2}}\left(\left(1+\sqrt{2}\right)\cos\beta + \sin\beta\right) - 12,$$

$$\eta_2 = \frac{9p}{\sqrt{2}}\left(\left(1-\sqrt{2}\right)\cos(3\beta) - \sin(3\beta)\right) + 2p^2(\cos(2\beta) + \sin(2\beta) - 2) + \frac{9p}{\sqrt{2}}\left(\left(1+\sqrt{2}\right)\cos\beta + \sin\beta\right) - 12,$$

$$\eta_3 = -\frac{3d}{\sqrt{2}}\left(\left(1-\sqrt{2}\right)\cos(3\beta) - \sin(3\beta)\right) + \frac{9d}{\sqrt{2}}\left(\left(1+\sqrt{2}\right)\cos\beta + \sin\beta\right) - 4pd(\cos(2\beta) + \sin(2\beta) + 2),$$

$$\eta_4 = \frac{3d}{\sqrt{2}}\left(\left(1-\sqrt{2}\right)\cos(3\beta) - \sin(3\beta)\right) + \frac{3d}{\sqrt{2}}\left(\left(1+\sqrt{2}\right)\cos\beta + \sin\beta\right),$$

$$\eta_5 = -2d^2(\cos(2\beta) + \sin(2\beta) + 2),$$

$$\eta_6 = \ 2d^2(\cos(2\beta) + \sin(2\beta) - 2),$$

$$\eta_7 = 3\sqrt{2}d\left(\left(1-\sqrt{2}\right)\cos(3\beta) - \sin(3\beta)\right) + 4pd(\cos(2\beta) + \sin(2\beta) - 2) + \ 3\sqrt{2}d\left(\left(1+\sqrt{2}\right)\cos\beta + \sin\beta\right),$$

$$\eta_8 = 2\sqrt{2}d\left(\cos\beta - \left(1+\sqrt{2}\right)\sin\beta\right) = \left(\frac{d}{p}\right)\eta_9,$$

$$\eta_{10} = -\frac{9p}{\sqrt{2}}\left(\cos(3\beta) + \left(1-\sqrt{2}\right)\sin(3\beta)\right) + 2p^2(\cos(2\beta) - \sin(2\beta)) + \frac{3p}{\sqrt{2}}\left(\cos\beta - \left(1+\sqrt{2}\right)\sin\beta\right),$$

$$\eta_{11} = \frac{3p}{\sqrt{2}}\left(\cos(3\beta) + \left(1-\sqrt{2}\right)\sin(3\beta)\right) + 2p^2(\sin(2\beta) - \cos(2\beta)) + \frac{3p}{\sqrt{2}}\left(\cos\beta - \left(1+\sqrt{2}\right)\sin\beta\right),$$

$$\eta_{12} = -\frac{3d}{\sqrt{2}}\left(\cos(3\beta) + \left(1-\sqrt{2}\right)\sin(3\beta)\right) + \frac{9d}{\sqrt{2}}\left(\cos\beta - \left(1+\sqrt{2}\right)\sin\beta\right),$$

$$\eta_{13} = \frac{3d}{\sqrt{2}}\left(\cos(3\beta) + \left(1-\sqrt{2}\right)\sin(3\beta)\right) - 4pd(\cos(2\beta) - \sin(2\beta)) + \frac{3d}{\sqrt{2}}\left(\cos\beta - \left(1+\sqrt{2}\right)\sin\beta\right),$$

$$\eta_{14} = 2d^2(\cos(2\beta) - \sin(2\beta)),$$

$$\eta_{15} = -3\sqrt{2}d\left(\cos(3\beta) + \left(1-\sqrt{2}\right)\sin(3\beta)\right) + 4pd(\cos(2\beta) - \sin(2\beta)) \\ - 3\sqrt{2}d\left(\cos\beta - \left(1+\sqrt{2}\right)\sin\beta\right).$$

Appendix B

The entries of the Jacobian matrix $\boldsymbol{J}$ of Eq (22), considering that $\psi_{xys} = \psi_{xs} - \psi_{ys}$:

$$J_{11} = -\frac{\zeta_r}{2} - \left(\frac{\varrho_1 + \varrho_3\omega_r^2}{8\omega_r}\right)a_{ys}^2\sin(2\psi_{xys}) - \left(\frac{\varrho_2}{8}\right)a_{ys}^2\cos(2\psi_{xys}) - \left(\frac{9\varrho_2}{8}\right)a_{xs}^2 - \left(\frac{\varrho_2}{4}\right)a_{ys}^2,$$

$$J_{12} = -\left(\frac{\varrho_1 + \varrho_3\omega_r^2}{4\omega_r}\right)a_{xs}a_{ys}^2\cos(2\psi_{xys}) + \left(\frac{\varrho_2}{4}\right)a_{xs}a_{ys}^2\sin(2\psi_{xys}) + \left(\frac{e\Omega^2}{2\omega_r}\right)\cos\psi_{xs},$$

$$J_{13} = -\left(\frac{\varrho_1 + \varrho_3\omega_r^2}{4\omega_r}\right)a_{xs}a_{ys}\sin(2\psi_{xys}) - \left(\frac{\varrho_2}{4}\right)a_{xs}a_{ys}\cos(2\psi_{xys}) - \left(\frac{\varrho_2}{2}\right)a_{xs}a_{ys},$$

$$J_{14} = \left(\frac{\varrho_1 + \varrho_3\omega_r^2}{4\omega_r}\right)a_{xs}a_{ys}^2\cos(2\psi_{xys}) - \left(\frac{\varrho_2}{4}\right)a_{xs}a_{ys}^2\sin(2\psi_{xys}),$$

$$J_{21} = -\left(\frac{3\varrho_1 + 3\gamma\omega_r^2}{4\omega_r}\right)a_{xs} - \left(\frac{e\Omega^2}{2\omega_r}\right)\frac{\cos\psi_{xs}}{a_{xs}^2},$$

$$J_{22} = \left(\frac{\varrho_1 + \varrho_3\omega_r^2}{4\omega_r}\right)a_{ys}^2\sin(2\psi_{xys}) + \left(\frac{\varrho_2}{4}\right)a_{ys}^2\cos(2\psi_{xys}) - \left(\frac{e\Omega^2}{2\omega_r}\right)\frac{\sin\psi_{xs}}{a_{xs}},$$

$$J_{23} = -\left(\frac{\varrho_1 + \varrho_3\omega_r^2}{4\omega_r}\right)a_{ys}\cos(2\psi_{xys}) + \left(\frac{\varrho_2}{4}\right)a_{ys}\sin(2\psi_{xys}) - \left(\frac{\varrho_1 + \varrho_3\omega_r^2}{4\omega_r}\right)a_{ys},$$

$$J_{24} = -\left(\frac{\varrho_1 + \varrho_3\omega_r^2}{4\omega_r}\right)a_{ys}^2\sin(2\psi_{xys}) - \left(\frac{\varrho_2}{4}\right)a_{ys}^2\cos(2\psi_{xys}),$$

$$J_{31} = \left(\frac{\varrho_1 + \varrho_3\omega_r^2}{4\omega_r}\right)a_{xs}a_{ys}\sin(2\psi_{xys}) - \left(\frac{\varrho_2}{4}\right)a_{xs}a_{ys}\cos(2\psi_{xys}) - \left(\frac{\varrho_2}{2}\right)a_{xs}a_{ys},$$

$$J_{32} = \left(\frac{\varrho_1 + \varrho_3\omega_r^2}{4\omega_r}\right)a_{xs}^2a_{ys}\cos(2\psi_{xys}) + \left(\frac{\varrho_2}{4}\right)a_{xs}^2a_{ys}\sin(2\psi_{xys}),$$

$$J_{33} = -\frac{\zeta_r}{2} + \left(\frac{\varrho_1 + \varrho_3\omega_r^2}{8\omega_r}\right)a_{xs}^2\sin(2\psi_{xys}) - \left(\frac{\varrho_2}{8}\right)a_{xs}^2\cos(2\psi_{xys}) - \left(\frac{9\varrho_2}{8}\right)a_{ys}^2 - \left(\frac{\varrho_2}{4}\right)a_{xs}^2,$$

$$J_{34} = -\left(\frac{\varrho_1 + \varrho_3\omega_r^2}{4\omega_r}\right)a_{xs}^2a_{ys}\cos(2\psi_{xys}) - \left(\frac{\varrho_2}{4}\right)a_{xs}^2a_{ys}\sin(2\psi_{xys}) + \left(\frac{e\Omega^2}{2\omega_r}\right)\sin\psi_{ys},$$

$$J_{41} = -\left(\frac{\varrho_1 - \varrho_3\omega_r^2}{4\omega_r}\right)a_{xs}\cos(2\psi_{xys}) - \left(\frac{\varrho_2}{4}\right)a_{xs}\sin(2\psi_{xys}) - \left(\frac{\varrho_1 + \varrho_3\omega_r^2}{2\omega_r}\right)a_{xs},$$

$$J_{42} = \left(\frac{\varrho_1 - \varrho_3\omega_r^2}{4\omega_r}\right)a_{xs}^2\sin(2\psi_{xys}) - \left(\frac{\varrho_2}{4}\right)a_{xs}^2\cos(2\psi_{xys}),$$

$$J_{43} = -\left(\frac{3\varrho_1 + 3\varrho_3\omega_r^2}{4\omega_r}\right)a_{ys} - \left(\frac{e\Omega^2}{2\omega_r}\right)\frac{\sin\psi_{ys}}{a_{ys}^2},$$

$$J_{44} = -\left(\frac{\varrho_1 - \varrho_3\omega_r^2}{4\omega_r}\right)a_{xs}^2\sin(2\psi_{xys}) + \left(\frac{\varrho_2}{4}\right)a_{xs}^2\cos(2\psi_{xys}) + \left(\frac{e\Omega^2}{2\omega_r}\right)\frac{\cos\psi_{ys}}{a_{ys}}.$$

The entries of the Jacobian matrix $\boldsymbol{L}$ of Eq (31), considering that $\psi_{xys} = \psi_{xs} - \psi_{ys}$:

$$L_{11} = -\frac{\zeta_c}{2} - \left(\frac{\eta_2 - \eta_6\omega_c^2}{8\omega_c}\right)a_{ys}^2\sin(2\psi_{xys}) - \left(\frac{\eta_{10} + 3\eta_{14}\omega_c^2}{4\omega_c}\right)a_{xs}a_{ys}\sin\psi_{xys} + \left(\frac{\eta_4 - \eta_7}{8}\right)a_{ys}^2\cos(2\psi_{xys}) - \left(\frac{\eta_{12} + \eta_{15}}{4}\right)a_{xs}a_{ys}\cos\psi_{xys} - \left(\frac{3\eta_3}{8}\right)a_{xs}^2 - \left(\frac{\eta_4}{4}\right)a_{ys}^2,$$

$$L_{12} = -\left(\frac{\eta_2 - \eta_6\omega_c^2}{4\omega_c}\right)a_{xs}a_{ys}^2\cos(2\psi_{xys}) - \left(\frac{\eta_{10} + 3\eta_{14}\omega_c^2}{8\omega_c}\right)a_{xs}^2a_{ys}\cos\psi_{xys} - \left(\frac{3\eta_{11} - \eta_{14}\omega_c^2}{8\omega_c}\right)a_{ys}^3\cos\psi_{xys} - \left(\frac{\eta_9}{2\omega_c}\right)a_{ys}\cos\psi_{xys} - \left(\frac{\eta_4 - \eta_7}{4}\right)a_{xs}a_{ys}^2\sin(2\psi_{xys}) + \left(\frac{\eta_{12} + \eta_{15}}{8}\right)a_{xs}^2a_{ys}\sin\psi_{xys} + \left(\frac{\eta_{13}}{8}\right)a_{ys}^3\sin\psi_{xys} + \left(\frac{\eta_8}{2}\right)a_{ys}\sin\psi_{xys} + \left(\frac{e\Omega^2}{2\omega_c}\right)\cos\psi_{xs},$$

$$L_{13} = -\left(\frac{\eta_2 - \eta_6\omega_c^2}{4\omega_c}\right)a_{xs}a_{ys}\sin(2\psi_{xys}) - \left(\frac{\eta_{10} + 3\eta_{14}\omega_c^2}{8\omega_c}\right)a_{xs}^2\sin\psi_{xys} - \left(\frac{9\eta_{11} - 3\eta_{14}\omega_c^2}{8\omega_c}\right)a_{ys}^2\sin\psi_{xys} - \left(\frac{\eta_9}{2\omega_c}\right)\sin\psi_{xys} + \left(\frac{\eta_4 - \eta_7}{4}\right)a_{xs}a_{ys}\cos(2\psi_{xys}) - \left(\frac{\eta_{12} + \eta_{15}}{8}\right)a_{xs}^2\cos\psi_{xys} - \left(\frac{3\eta_{13}}{8}\right)a_{ys}^2\cos\psi_{xys} - \left(\frac{\eta_8}{2}\right)\cos\psi_{xys} - \left(\frac{\eta_4}{2}\right)a_{xs}a_{ys},$$

$$L_{14} = \left(\frac{\eta_2 - \eta_6\omega_c^2}{4\omega_c}\right)a_{xs}a_{ys}^2\cos(2\psi_{xys}) + \left(\frac{\eta_{10} + 3\eta_{14}\omega_c^2}{8\omega_c}\right)a_{xs}^2a_{ys}\cos\psi_{xys} + \left(\frac{3\eta_{11} - \eta_{14}\omega_c^2}{8\omega_c}\right)a_{ys}^3\cos\psi_{xys} + \left(\frac{\eta_9}{2\omega_c}\right)a_{ys}\cos\psi_{xys} + \left(\frac{\eta_4 - \eta_7}{4}\right)a_{xs}a_{ys}^2\sin(2\psi_{xys}) - \left(\frac{\eta_{12} + \eta_{15}}{8}\right)a_{xs}^2a_{ys}\sin\psi_{xys} - \left(\frac{\eta_{13}}{8}\right)a_{ys}^3\sin\psi_{xys} - \left(\frac{\eta_8}{2}\right)a_{ys}\sin\psi_{xys},$$

$$L_{21} = -\left(\frac{3\eta_{10} + \eta_{14}\omega_c^2}{8\omega_c}\right)a_{ys}\cos\psi_{xys} + \left(\frac{3\eta_{11} - \eta_{14}\omega_c^2}{8\omega_c}\right)\frac{a_{ys}^3\cos\psi_{xys}}{a_{xs}^2} + \left(\frac{\eta_9}{2\omega_c}\right)\frac{a_{ys}\cos\psi_{xys}}{a_{xs}^2} - \left(\frac{3\eta_{12} + \eta_{15}}{8}\right)a_{ys}\sin\psi_{xys} - \left(\frac{\eta_{13}}{8}\right)\frac{a_{ys}^3\sin\psi_{xys}}{a_{xs}^2} - \left(\frac{\eta_8}{2}\right)\frac{a_{ys}\sin\psi_{xys}}{a_{xs}^2} - \left(\frac{3\eta_1 + \eta_5\omega_c^2}{4\omega_c}\right)a_{xs} - \left(\frac{e\Omega^2}{2\omega_c}\right)\frac{\cos\psi_{xs}}{a_{xs}^2},$$

$$L_{22} = \left(\frac{\eta_2 - \eta_6\omega_c^2}{4\omega_c}\right) a_{ys}^2 \sin(2\psi_{xys}) + \left(\frac{3\eta_{10} + \eta_{14}\omega_c^2}{8\omega_c}\right) a_{xs}a_{ys} \sin\psi_{xys} + \left(\frac{3\eta_{11} - \eta_{14}\omega_c^2}{8\omega_c}\right)\frac{a_{ys}^3 \sin\psi_{xys}}{a_{xs}} + \left(\frac{\eta_9}{2\omega_c}\right)\frac{a_{ys}\sin\psi_{xys}}{a_{xs}} - \left(\frac{\eta_4 - \eta_7}{4}\right) a_{ys}^2 \cos(2\psi_{xys}) - \left(\frac{3\eta_{12} + \eta_{15}}{8}\right) a_{xs}a_{ys}\cos\psi_{xys} + \left(\frac{\eta_{13}}{8}\right)\frac{a_{ys}^3\cos\psi_{xys}}{a_{xs}} + \left(\frac{\eta_8}{2}\right)\frac{a_{ys}\cos\psi_{xys}}{a_{xs}} - \left(\frac{e\Omega^2}{2\omega_c}\right)\frac{\sin\psi_{xs}}{a_{xs}},$$

$$L_{23} = -\left(\frac{\eta_2 - \eta_6\omega_c^2}{4\omega_c}\right) a_{ys}\cos(2\psi_{xys}) - \left(\frac{3\eta_{10} + \eta_{14}\omega_c^2}{8\omega_c}\right) a_{xs}\cos\psi_{xys} - \left(\frac{9\eta_{11} - 3\eta_{14}\omega_c^2}{8\omega_c}\right)\frac{a_{ys}^2\cos\psi_{xys}}{a_{xs}} - \left(\frac{\eta_9}{2\omega_c}\right)\frac{\cos\psi_{xys}}{a_{xs}} - \left(\frac{\eta_4 - \eta_7}{4}\right) a_{ys}\sin(2\psi_{xys}) - \left(\frac{3\eta_{12} + \eta_{15}}{8}\right) a_{xs}\sin\psi_{xys} + \left(\frac{3\eta_{13}}{8}\right)\frac{a_{ys}^2\sin\psi_{xys}}{a_{xs}} + \left(\frac{\eta_8}{2}\right)\frac{\sin\psi_{xys}}{a_{xs}} - \left(\frac{\eta_2 + \eta_6\omega_c^2}{2\omega_c}\right) a_{ys},$$

$$L_{24} = -\left(\frac{\eta_2 - \eta_6\omega_c^2}{4\omega_c}\right) a_{ys}^2 \sin(2\psi_{xys}) - \left(\frac{3\eta_{10} + \eta_{14}\omega_c^2}{8\omega_c}\right) a_{xs}a_{ys}\sin\psi_{xys} - \left(\frac{3\eta_{11} - \eta_{14}\omega_c^2}{8\omega_c}\right)\frac{a_{ys}^3\sin\psi_{xys}}{a_{xs}} - \left(\frac{\eta_9}{2\omega_c}\right)\frac{a_{ys}\sin\psi_{xys}}{a_{xs}} + \left(\frac{\eta_4 - \eta_7}{4}\right) a_{ys}^2\cos(2\psi_{xys}) + \left(\frac{3\eta_{12} + \eta_{15}}{8}\right) a_{xs}a_{ys}\cos\psi_{xys} - \left(\frac{\eta_{13}}{8}\right)\frac{a_{ys}^3\cos\psi_{xys}}{a_{xs}} - \left(\frac{\eta_8}{2}\right)\frac{a_{ys}\cos\psi_{xys}}{a_{xs}},$$

$$L_{31} = \left(\frac{\eta_2 - \eta_6\omega_c^2}{4\omega_c}\right) a_{xs}a_{ys}\sin(2\psi_{xys}) - \left(\frac{\eta_{10} + 3\eta_{14}\omega_c^2}{8\omega_c}\right) a_{ys}^2\sin\psi_{xys} - \left(\frac{9\eta_{11} - 3\eta_{14}\omega_c^2}{8\omega_c}\right) a_{xs}^2\sin\psi_{xys} - \left(\frac{\eta_9}{2\omega_c}\right)\sin\psi_{xys} + \left(\frac{\eta_4 - \eta_7}{4}\right) a_{xs}a_{ys}\cos(2\psi_{xys}) + \left(\frac{\eta_{12} + \eta_{15}}{8}\right) a_{ys}^2\cos\psi_{xys} + \left(\frac{3\eta_{13}}{8}\right) a_{xs}^2\cos\psi_{xys} + \left(\frac{\eta_8}{2}\right)\cos\psi_{xys} - \left(\frac{\eta_4}{2}\right) a_{xs}a_{ys},$$

$$L_{32} = \left(\frac{\eta_2 - \eta_6\omega_c^2}{4\omega_c}\right) a_{xs}^2 a_{ys}\cos(2\psi_{xys}) - \left(\frac{\eta_{10} + 3\eta_{14}\omega_c^2}{8\omega_c}\right) a_{xs}a_{ys}^2\cos\psi_{xys} - \left(\frac{3\eta_{11} - \eta_{14}\omega_c^2}{8\omega_c}\right) a_{xs}^3\cos\psi_{xys} - \left(\frac{\eta_9}{2\omega_c}\right) a_{xs}\cos\psi_{xys} - \left(\frac{\eta_4 - \eta_7}{4}\right) a_{xs}^2 a_{ys}\sin(2\psi_{xys}) - \left(\frac{\eta_{12} + \eta_{15}}{8}\right) a_{xs}a_{ys}^2\sin\psi_{xys} - \left(\frac{\eta_{13}}{8}\right) a_{xs}^3\sin\psi_{xys} - \left(\frac{\eta_8}{2}\right) a_{xs}\sin\psi_{xys},$$

$$L_{33} = -\frac{\zeta_c}{2} + \left(\frac{\eta_2 - \eta_6\omega_c^2}{8\omega_c}\right) a_{xs}^2\sin(2\psi_{xys}) - \left(\frac{\eta_{10} + 3\eta_{14}\omega_c^2}{4\omega_c}\right) a_{xs}a_{ys}\sin\psi_{xys} + \left(\frac{\eta_4 - \eta_7}{8}\right) a_{xs}^2\cos(2\psi_{xys}) + \left(\frac{\eta_{12} + \eta_{15}}{4}\right) a_{xs}a_{ys}\cos\psi_{xys} - \left(\frac{3\eta_3}{8}\right) a_{ys}^2 - \left(\frac{\eta_4}{4}\right) a_{xs}^2,$$

$$L_{34} = -\left(\frac{\eta_2 - \eta_6\omega_c^2}{4\omega_c}\right)a_{xs}^2 a_{ys}\cos(2\psi_{xys}) + \left(\frac{\eta_{10} + 3\eta_{14}\omega_c^2}{8\omega_c}\right)a_{xs}a_{ys}^2\cos\psi_{xys}$$
$$+ \left(\frac{3\eta_{11} - \eta_{14}\omega_c^2}{8\omega_c}\right)a_{xs}^3\cos\psi_{xys} + \left(\frac{\eta_9}{2\omega_c}\right)a_{xs}\cos\psi_{xys}$$
$$+ \left(\frac{\eta_4 - \eta_7}{4}\right)a_{xs}^2 a_{ys}\sin(2\psi_{xys}) + \left(\frac{\eta_{12} + \eta_{15}}{8}\right)a_{xs}a_{ys}^2\sin\psi_{xys} + \left(\frac{\eta_{13}}{8}\right)a_{xs}^3\sin\psi_{xys}$$
$$+ \left(\frac{\eta_8}{2}\right)a_{xs}\sin\psi_{xys} + \left(\frac{e\Omega^2}{2\omega_c}\right)\sin\psi_{ys},$$

$$L_{41} = -\left(\frac{\eta_2 - \eta_6\omega_c^2}{4\omega_c}\right)a_{xs}\cos(2\psi_{xys}) + \left(\frac{3\eta_{10} + \eta_{14}\omega_c^2}{8\omega_c}\right)a_{ys}\cos\psi_{xys}$$
$$+ \left(\frac{9\eta_{11} - 3\eta_{14}\omega_c^2}{8\omega_c}\right)\frac{a_{xs}^2\cos\psi_{xys}}{a_{ys}} + \left(\frac{\eta_9}{2\omega_c}\right)\frac{\cos\psi_{xys}}{a_{ys}} + \left(\frac{\eta_4 - \eta_7}{4}\right)a_{xs}\sin(2\psi_{xys})$$
$$+ \left(\frac{3\eta_{12} - \eta_{15}}{8}\right)a_{ys}\sin\psi_{xys} + \left(\frac{3\eta_{13}}{8}\right)\frac{a_{xs}^2\sin\psi_{xys}}{a_{ys}} + \left(\frac{\eta_8}{2}\right)\frac{\sin\psi_{xys}}{a_{ys}}$$
$$- \left(\frac{\eta_2 + \eta_6\omega_c^2}{2\omega_c}\right)a_{xs},$$

$$L_{42} = \left(\frac{\eta_2 - \eta_6\omega_c^2}{4\omega_c}\right)a_{xs}^2\sin(2\psi_{xys}) - \left(\frac{3\eta_{10} + \eta_{14}\omega_c^2}{8\omega_c}\right)a_{xs}a_{ys}\sin\psi_{xys}$$
$$- \left(\frac{3\eta_{11} - \eta_{14}\omega_c^2}{8\omega_c}\right)\frac{a_{xs}^3\sin\psi_{xys}}{a_{ys}} - \left(\frac{\eta_9}{2\omega_c}\right)\frac{a_{xs}\sin\psi_{xys}}{a_{ys}} + \left(\frac{\eta_4 - \eta_7}{4}\right)a_{xs}^2\cos(2\psi_{xys})$$
$$+ \left(\frac{3\eta_{12} - \eta_{15}}{8}\right)a_{xs}a_{ys}\cos\psi_{xys} + \left(\frac{\eta_{13}}{8}\right)\frac{a_{xs}^3\cos\psi_{xys}}{a_{ys}} + \left(\frac{\eta_8}{2}\right)\frac{a_{xs}\cos\psi_{xys}}{a_{ys}},$$

$$L_{43} = \left(\frac{3\eta_{10} + \eta_{14}\omega_c^2}{8\omega_c}\right)a_{xs}\cos\psi_{xys} - \left(\frac{3\eta_{11} - \eta_{14}\omega_c^2}{8\omega_c}\right)\frac{a_{xs}^3\cos\psi_{xys}}{a_{ys}^2} - \left(\frac{\eta_9}{2\omega_c}\right)\frac{a_{xs}\cos\psi_{xys}}{a_{ys}^2}$$
$$+ \left(\frac{3\eta_{12} - \eta_{15}}{8}\right)a_{xs}\sin\psi_{xys} - \left(\frac{\eta_{13}}{8}\right)\frac{a_{xs}^3\sin\psi_{xys}}{a_{ys}^2} - \left(\frac{\eta_8}{2}\right)\frac{a_{xs}\sin\psi_{xys}}{a_{ys}^2}$$
$$- \left(\frac{3\eta_1 + \eta_5\omega_c^2}{4\omega_c}\right)a_{ys} - \left(\frac{e\Omega^2}{2\omega_c}\right)\frac{\sin\psi_{ys}}{a_{ys}^2},$$

$$L_{44} = -\left(\frac{\eta_2 - \eta_6\omega_c^2}{4\omega_c}\right)a_{xs}^2\sin(2\psi_{xys}) + \left(\frac{3\eta_{10} + \eta_{14}\omega_c^2}{8\omega_c}\right)a_{xs}a_{ys}\sin\psi_{xys}$$
$$+ \left(\frac{3\eta_{11} - \eta_{14}\omega_c^2}{8\omega_c}\right)\frac{a_{xs}^3\sin\psi_{xys}}{a_{ys}} + \left(\frac{\eta_9}{2\omega_c}\right)\frac{a_{xs}\sin\psi_{xys}}{a_{ys}} - \left(\frac{\eta_4 - \eta_7}{4}\right)a_{xs}^2\cos(2\psi_{xys})$$
$$- \left(\frac{3\eta_{12} - \eta_{15}}{8}\right)a_{xs}a_{ys}\cos\psi_{xys} - \left(\frac{\eta_{13}}{8}\right)\frac{a_{xs}^3\cos\psi_{xys}}{a_{ys}} - \left(\frac{\eta_8}{2}\right)\frac{a_{xs}\cos\psi_{xys}}{a_{ys}}$$
$$+ \left(\frac{e\Omega^2}{2\omega_c}\right)\frac{\cos\psi_{ys}}{a_{ys}}.$$

Appendix C

The derivation of Eqs (8) and (9) can be as follows:
Substituting Eqs (4) and (7) into Eq (3) gives us

$$F_n = K\left(\frac{I_0 - (g_1 x + g_2 \dot{x})\, cos\big((n-1)\alpha + \beta\big) - (g_1 y + g_2 \dot{y})\, sin\big((n-1)\alpha + \beta\big)}{C_0 - x\, cos\big((n-1)\alpha + \beta\big) - y\, sin\big((n-1)\alpha + \beta\big)}\right)^2, \tag{C1}$$

where $n = 1,2,\ldots,8$. Inserting Eq (C1) into Eqs (5) and (6) yields

$$R_x = K\sum_{j=1}^{8}\left(\frac{I_0 - (g_1 x + g_2 \dot{x})\, cos\big((j-1)\alpha + \beta\big) - (g_1 y + g_2 \dot{y})\, sin\big((j-1)\alpha + \beta\big)}{C_0 - x\, cos\big((j-1)\alpha + \beta\big) - y\, sin\big((j-1)\alpha + \beta\big)}\right)^2 \cos\big((j-1)\alpha + \beta\big), \tag{C2}$$

$$R_y = K\sum_{j=1}^{8}\left(\frac{I_0 - (g_1 x + g_2 \dot{x})\, cos\big((j-1)\alpha + \beta\big) - (g_1 y + g_2 \dot{y})\, sin\big((j-1)\alpha + \beta\big)}{C_0 - x\, cos\big((j-1)\alpha + \beta\big) - y\, sin\big((j-1)\alpha + \beta\big)}\right)^2 \sin\big((j-1)\alpha + \beta\big). \tag{C3}$$

Approximating R_x and R_y in Eqs (C2) and (C3) with Taylor series near the origin ($x = y = 0$) up to the third order is

$$R_x \approx A_1 x + A_2 \dot{x} + A_3(x^3 + xy^2) + A_4(\dot{x}y^2 + 2xy\dot{y} + 3x^2\dot{x}) + A_5(x\dot{y}^2 + 2\dot{x}y\dot{y} + 3x\dot{x}^2), \tag{C4}$$

$$R_y \approx A_1 y + A_2 \dot{y} + A_3(y^3 + x^2 y) + A_4(x^2\dot{y} + 2x\dot{x}y + 3y^2\dot{y}) + A_5(\dot{x}^2 y + 2x\dot{x}\dot{y} + 3y\dot{y}^2), \tag{C5}$$

where

$$A_1 = \frac{8KI_0(I_0 - C_0 g_1)}{C_0^3},$$

$$A_2 = -\frac{8KI_0 g_2}{C_0^2},$$

$$A_3 = \frac{8K}{C_0^5}\left(\cos^4\left(\frac{\pi}{4} + \beta\right) + \cos^4\beta - \cos^2\left(\frac{\pi}{4} + \beta\right) - \cos^2\beta + 1\right)(-C_0 g_1 + 2I_0)(-C_0 g_1 + I_0),$$

$$A_4 = -\frac{16Kg_2}{C_0^4}\left(\cos^4\left(\frac{\pi}{4} + \beta\right) + \cos^4\beta - \cos^2\left(\frac{\pi}{4} + \beta\right) - \cos^2\beta\right)\left(C_0 g_1 - \frac{3}{2}I_0\right),$$

$$A_5 = -\frac{8Kg_2^2}{C_0^3}\left(\cos^4\left(\frac{\pi}{4} + \beta\right) + \cos^4\beta - \cos^2\left(\frac{\pi}{4} + \beta\right) - \cos^2\beta\right).$$

Inserting Eqs (C4) and (C5) into Eqs (1) and (2) and simplifying yield

$$\begin{aligned}\ddot{x} + \left(\frac{\delta - A_2}{M}\right)\dot{x} - \frac{A_1}{M}x - \frac{A_3}{M}(x^3 + xy^2) - \frac{A_4}{M}(\dot{x}y^2 + 2xy\dot{y} + 3x^2\dot{x}) \\ - \frac{A_5}{M}(x\dot{y}^2 + 2\dot{x}y\dot{y} + 3x\dot{x}^2) = E\Omega^2\cos(\Omega t),\end{aligned} \tag{C6}$$

$$\begin{aligned}\ddot{y} + \left(\frac{\delta - A_2}{M}\right)\dot{y} - \frac{A_1}{M}y - \frac{A_3}{M}(y^3 + x^2 y) - \frac{A_4}{M}(x^2\dot{y} + 2x\dot{x}y + 3y^2\dot{y}) \\ - \frac{A_5}{M}(\dot{x}^2 y + 2x\dot{x}\dot{y} + 3y\dot{y}^2) = E\Omega^2\sin(\Omega t).\end{aligned} \tag{C7}$$

We can normalize the quantities x and y to get the dimensionless quantities $\hat{x}$ and $\hat{y}$ by making them relative to C_0 such that $\hat{x} = x/C_0$ and $\hat{y} = y/C_0$. Accordingly, we can continue the

time normalization process to get the dimensionless time $\hat{t}$ such that $\hat{t} = t/B$ and $\widehat{\Omega} = B\Omega$ where $B^2 = KMC_0^3 I_0^{-2}$. The hats will be omitted later for simplicity. Doing so, then simplifying, gives us

$$\ddot{x} + \zeta_r \dot{x} + \omega_r^2 x + \varrho_1(x^3 + xy^2) + \varrho_2(\dot{x}y^2 + 2xy\dot{y} + 3x^2\dot{x}) + \varrho_3(x\dot{y}^2 + 2\dot{x}y\dot{y} + 3x\dot{x}^2) = e\Omega^2 \cos(\Omega t), \tag{C8}$$

$$\ddot{y} + \zeta_r \dot{y} + \omega_r^2 y + \varrho_1(y^3 + x^2 y) + \varrho_2(x^2\dot{y} + 2x\dot{x}y + 3y^2\dot{y}) + \varrho_3(\dot{x}^2 y + 2x\dot{x}\dot{y} + 3y\dot{y}^2) = e\Omega^2 \sin(\Omega t)\,, \tag{C9}$$

where the parameters e, ζ_r, ω_r^2, ϱ_1, ϱ_2, and ϱ_3 are given in Appendix A. Equations (C8) and (C9) are Eqs (8) and (9) given in Section 2.